Mammalian ATG8 proteins maintain autophagosomal membrane integrity through ESCRTs

Ruheena Javed[1,2], Ashish Jain[3], Thabata Duque[1,2], Emily Hendrix[4], Masroor Ahmad Paddar[1,2], Sajjad Khan[5], Aurore Claude-Taupin[2], Jingyue Jia[1,2], Lee Allers[1,2], Fulong Wang[1,2], Michal Mudd[1,2], Graham Timmins[2], Keith Lidke[5], Tor Erik Rusten[3], Prithvi Reddy Akepati [8], Yi He[4], Fulvio Reggiori[6,7], Eeva-Liisa Eskelinen[9]*, and Vojo Deretic[1,2,*,**]

[1] Department of Molecular Genetics and Microbiology, University of New Mexico Health Sciences Center, 915 Camino de Salud, NE, Albuquerque, NM 87131, USA
[2] Autophagy, Inflammation and Metabolism Center of Biochemical Research Excellence, University of New Mexico Health Sciences Center, Albuquerque, USA
[3] Faculty of Medicine, University of Oslo, Oslo, Norway
[4] Department of Chemistry & Chemical Biology, The University of New Mexico, Albuquerque, New Mexico 87131, USA
[5] Department of Physics and Astronomy, The University of New Mexico, Albuquerque, New Mexico 87131, USA
[6] Department of Biomedicine and [7] Aarhus Institute for Advanced Studies (AIAS), Aarhus University, Denmark
[8] Division of Gastroenterology and Hepatology, Department of Internal Medicine, University of New Mexico, Albuquerque, New Mexico 87131, USA
[9] Institute of Biomedicine, University of Turku, Finland

* Co-corresponding authors

**Lead author:
Vojo Deretic, Ph.D.
Department of Molecular Genetics and Microbiology
University of New Mexico Health Sciences Center
915 Camino de Salud, NE
Albuquerque, NM 87131, U.S.A.
vderetic@salud.unm.edu

Abstract

The canonical autophagy pathway in mammalian cells sequesters diverse cytoplasmic cargo within the double membrane autophagosomes that eventually convert into degradative compartments via fusion with endolysosomal intermediates. Here we report the discovery of a porousness of autophagosomal membranes in cells lacking principal ATG8 proteins (mATG8s) and that they are unable to mature into autolysosomes. Using a combination of methods including a novel in vitro assay, we uncovered a previously unappreciated function of mATG8s which act to maintain autophagosomal membranes in a sealed state. The mATG8 proteins GABARAP and LC3A bind to the key ESCRT-I components contributing, along with other ESCRTs, to the integrity and imperviousness of autophagic membranes. The autophagic organelles in cells lacking mATG8s are permeant, are arrested as amphisomes, and do not progress to functional autolysosomes. Thus, autophagosomal organelles need to be maintained in a sealed state in order to become lytic autolysosomes.

Introduction

Autophagy represents a collection of processes sequestering diverse cytoplasmic cargo destined for removal or recycling through degradation (Deretic & Lazarou, 2022; Dong *et al*, 2021; Mizushima *et al*, 2008), with the cargo vastly varied in composition, shape, and size (Chang *et al*, 2021). Canonical autophagy in mammalian cells (Levine & Kroemer, 2019; Morishita & Mizushima, 2019) plays multiple roles in cellular metabolism (Deretic & Kroemer, 2021; Lahiri *et al*, 2019), cytoplasmic quality control (Levine & Kroemer, 2019), anti-inflammatory processes (Deretic, 2021), and has been implicated in numerous fundamental and disease-related processes (Klionsky *et al*, 2021; Mizushima & Levine, 2020).

Canonical autophagy progresses through sequential stages including cytoplasmic emergence of double membrane organelles termed autophagosomes (Morishita & Mizushima, 2019). The process of mammalian autophagosomal formation engages membrane sources from ER (Axe *et al*, 2008; Hara *et al*, 2008; Hayashi-Nishino *et al*, 2009; Itakura & Mizushima, 2010, 2011; Mizushima *et al*, 2011; Nishimura *et al*, 2017; Tooze & Yoshimori, 2010) and endosomes (Knaevelsrud *et al*, 2013; Longatti *et al*, 2012; Moreau *et al*, 2011; Puri *et al*, 2013; Puri *et al*, 2018; Ravikumar *et al*, 2010; Soreng *et al*, 2018). Other parts of the early secretory pathway are involved including ER-Golgi intermediate compartment (Ge *et al*, 2013; Ge *et al*, 2017; Ge *et al*, 2014) culminating in fusion of such membranes (Kumar *et al*, 2019; Kumar *et al*, 2021a) to form prophagophores (Deretic & Lazarou, 2022). Prophagophores progress into phagophores by membrane modification with mammalian ATG8 proteins (mATG8s). One of these, LC3B, represents a widely used autophagy marker (Kabeya *et al*, 2000). Phagophores expand via the action of multiple factors including lipid transfer proteins (Valverde *et al*, 2019) and lipid scramblases including ATG9A (Ghanbarpour *et al*, 2021; Maeda *et al*, 2020; Matoba *et al*, 2020). The phagophores eventually close into a double membrane autophagosome to sequester the cargo. Whereas autophagosomes fuse with the vacuole in yeast (Zhao & Zhang, 2019), mammalian autophagosomes continue to interact and fuse with the organelles of the endolysosomal system (Gordon & Seglen, 1988). Multivesicular bodies endosomes (MVB)/late endosomes containing intraluminal vesicles are a typical fusion partner for autophagosomes to form amphisomes (Berg *et al*, 1998; Eskelinen *et al*, 2002; Liou *et al*, 1997). These autophagic intermediates further mature acquiring lysosomal characteristics and progress into degradative autolysosomes (Zhao & Zhang, 2019).

The final steps of the autophagosome completion are believed to involve phagophore closure through a membrane scission process catalyzed by ESCRT proteins (Flower *et al*, 2020; Knorr *et al*, 2015; Takahashi *et al*, 2018; Takahashi *et al*, 2019; Zhen *et al*, 2020). Several ESCRTs have been identified in these processes including ESCRT-I (Flower *et al.*, 2020; Takahashi *et al.*, 2019) and ESCRT-III components (Takahashi *et al.*, 2018; Zhen *et al.*, 2020). Of note, these proteins play roles in other ESCRT-dependent processes (Christ *et al*, 2017; Hurley, 2015) including maintenance of membrane integrity through repair (Zhen *et al*, 2021). How ESCRTs are recruited to the closing phagophores, if this occurs at a single point or multiple locations,

whether the autophagosomes themselves are subject to homeostasis, and if their membranes need to be actively maintained, is not known.

One of the hallmarks of autophagy is the lipidation (Mizushima, 2020; Mizushima *et al.*, 2011) of mATG8s (He *et al*, 2003; Weidberg *et al*, 2010; Xin *et al*, 2001). There are two classes (Weidberg *et al.*, 2010) of mATG8s: LC3s (LC3A, LC3B, LC3C) and GABARAPs (GABARAP, GABARAPL1, and GABARAPL2). The mATG8s lipidation cascade, first delineated in yeast with Atg8 (Ichimura *et al*, 2000; Mizushima *et al*, 1998), results in atg8ylation (Deretic & Lazarou, 2022) of prophagophores. Whereas LC3B is commonly used to identify autophagosomes (Kabeya *et al.*, 2000) it can be present on single membranes other than autophagosomes (Galluzzi & Green, 2019; Goodwin *et al*, 2021; Guo *et al*, 2017; Kumar *et al*, 2020; Kumar *et al*, 2021b; Lee *et al*, 2020; Leidal *et al*, 2020; Loi *et al*, 2019; Nakamura *et al*, 2020; Sanjuan *et al*, 2007; Ulferts *et al*, 2021). The best understood function of mATG8s is the enhancement of cargo sequestration into autophagosomes (Lamark & Johansen, 2021; Randow & Youle, 2014; Stolz *et al*, 2014) with additional functions proposed in membrane remodeling (Weidberg *et al*, 2011), membrane perturbation (Maruyama *et al*, 2021) during autophagosome biogenesis, autophagosome-lysosome fusion (Weidberg *et al.*, 2010), and in membrane stress responses (Kumar *et al.*, 2021b). Autophagosomes can nevertheless form in cells lacking all principal mATG8s (Nguyen *et al*, 2016; Nguyen *et al*, 2021) or in cells defective for mATG8 lipidation (Ohnstad *et al*, 2020), albeit their size (Nguyen *et al.*, 2016) or composition (Ohnstad *et al.*, 2020) and possibly quality are affected.

Recently, an assay directly measuring autophagosomal state using small molecular weight probes relying on HaloTag-LC3B (HT-LC3B) and its fluorescent ligands to differentiate autophagosomes with membranes remaining permeant or becoming impermeant to such probes has been developed (Flower *et al.*, 2020; Takahashi *et al.*, 2018; Takahashi *et al.*, 2019). Using this system and a novel in vitro assay established here, we report that mATG8s play a key role in directing specific ESCRT proteins to autophagosomes in order to maintain their membranes sealed and impermeant and thus allowing them to progress into degradative compartments.

Results

Mammalian ATG8 proteins affect permeability of autophagic membranes

The mATG8 proteins participate in canonical and non-canonical processes associated with autophagy and in activities independent of autophagy (Deretic & Lazarou, 2022). During canonical autophagy, mATG8s affect autophagosomal membrane expansion and size (Nguyen *et al.*, 2016), interactions with autophagic cargo receptors (Lamark & Johansen, 2021; Randow & Youle, 2014; Stolz *et al.*, 2014), membrane perturbations (Maruyama *et al.*, 2021), and display a kinetic effects on autophagosome-lysosome fusion (Tsuboyama *et al*, 2016). Given a broad spectrum of mATG8s' roles, many of which fall under the category of quality control, and the likely perturbations associated with autophagic membrane growth, expansion and completion, we wondered whether they affected the physical properties of autophagosomal membranes such as permeability to molecules.

To approach this question, we used the previously described strategy (Takahashi *et al.*, 2018) employing stable cell lines expressing HT-LC3B, used initially in studies of autophagosomal completion (Flower *et al.*, 2020; Takahashi *et al.*, 2018; Takahashi *et al.*, 2019) but in principle applicable to probing autophagic membrane integrity and permeability in general. We adapted this assay for high content microscopy (HCM) to allow unbiased operator-independent image collection, object identification and quantification, as previously established (Jia *et al*, 2018; Kumar *et al.*, 2021a) (Fig 1A; MPL-MIL HCM assay). For this, isogenic cell lines, parental $HeLa^{WT}$ and its derivative $HeLa^{HexaKO}$ with inactivated 6 mATG8s (LC3A,B,C, and GABARAP, L1, L2; $HeLa^{HexaKO}$) (Nguyen *et al.*, 2016) were modified to stably express HT-LC3B. Cells were seeded in 96 well plates, starved for 90 min in EBSS to induce autophagy, subjected to selective plasma membrane (PM) permeabilization with a commercial PM membrane permeabilizer (PMP; Agilent), as originally reported (Flower *et al.*, 2020; Takahashi *et al.*, 2018; Takahashi *et al.*, 2019), and sequentially stained with fluorescent HaloTag ligands that covalently modify haloalkane dehalogenase (Takahashi *et al.*, 2018). First, the membrane impermeant ligand (MIL), a compound with haloalkane dehalogenase-reactive linker and fluorescent reporter Alexa Fluor 660 fluorescing at 690 nm (pseudocolored as green), was applied to unfixed cells to serve as a reporter for unsealed autophagosomes (Takahashi *et al.*, 2018). The initial exposure to the MIL ligand saturates all accessible haloalkane dehalogenase HT-LC3B molecules except those that are inaccessible by being sequestered away from the cytosol, such as the ones enclosed within autophagosomes (Takahashi *et al.*, 2018). The HT-LC3B molecules that remained inaccessible to MIL within sealed autophagosomal membranes or sequestered in other endomembranes are then revealed by staining with membrane permeant ligand (MPL), a compound containing haloalkane dehalogenase-reactive linker with tetramethylrhodamine (TMR) fluorescing at 585 nm (colored red). The plates were scanned to quantify MPL^+ (membranes without openings, impermeant to the MIL probe) and MIL^+ (membranes with openings, permeant to the MIL probe) autophagosomes and any additional $LC3B^+$ structures, and data (quantitative HCM) presented as the number of MPL^+ or MIL^+ profiles/cell and their ratios (MIL/MPL) (Fig

1B). Although double positive MPL^+ MIL^+ profiles were also observed, they represented a very small fraction (<5%) and were not studied further or differentiated in quantifications. Both MPL^+ and MIL^+ profiles increased with starvation in $HeLa^{WT}$ HT-LC3B cells, whereas MPL^+ but not the MIL^+ profiles were further elevated in starved cells treated with bafilomycin A1 (BafA1) (Fig 1B, subpanels i and ii), consistent with MPL^+ profiles being competent for progression into autolysosomes. When compared to $HeLa^{WT}$ HT-LC3B cells, $HeLa^{HexaKO}$ HT-LC3B cells showed a decrease in MPL^+ profiles and a further increase in MIL^+ profiles with (Fig 1B, subpanels i and ii). This was reflected in elevated ratios of MIL vs MPL profile numbers/cell in $HeLa^{HexaKO}$ vs $HeLa^{WT}$ cells (Fig 1B, subpanel iii). Similar relationships were observed with digitonin, used as a selective PM permeabilizing agent, in side-by-side comparisons with PMP (Fig EV1A,B). The specificity was further established by staining cells (incubated in full medium or EBSS) without PM permeabilization, whence no MIL staining was observed (Fig EV1B, subpanel i). Increased MIL/MPL ratios were observed in $HeLa^{HexaKO}$ cells subjected to PM permeabilization with PMP or digitonin, in keeping with MIL accessing HT-LC3B only when PM was selectively permeabilized (Fig EV1B, subpanel iii). This was not the case with general membrane permeabilization agents saponin or TX-100, which permeabilize endomembranes in addition to PM, allowing MIL to saturate the majority of HT-LC3B sites including those within the interior aspects of autophagosomes (Appendix Fig S1A,B). In the standard protocol with PMP, the diminished numbers of MPL^+ profiles in $HeLa^{HexaKO}$ HT-LC3B cells relative to $HeLa^{WT}$ HT-LC3B cells could not be enhanced by BafA1 treatment, excluding an increase in autophagic turn-over as a potential explanation (Fig 1B, subpanel i), also observed with digitonin as a permeabilizing agent (Fig EV1B subpanel ii). Of note, expression of the HT-LC3B transgene in HeLa cells devoid of the six principal mATG8s ($HeLa^{HexaKO}$) did not complement the high-MIL^+ low- MPL^+ phenotype (Nguyen *et al.*, 2016).

These findings show that mATG8s are important to maintain $LC3B^+$ membranes both impermeant to small probes (such as MIL) and in a state competent for progression to autolysosome.

Ultrastructural analysis of organelles in cells devoid of the principal mATG8s

Given that the MPL-MIL HCM assay data suggest that absence of mATG8s compromises the quality/integrity of autophagic membranes, we carried out electron microscopy (EM), immuno-EM and super-resolution (SR) analyses to morphologically examine autophagic organelles. The EM studies (Fig 1C-E) revealed that in the absence of mATG8s in $HeLa^{HexaKO}$, there was an accumulation of organelles morphologically identified as amphisomes, accompanied by a reduction in more mature, degradative autolysosomes (Fig 1E). The accumulating structures of amphisomal ultrastructural morphology (Fig 1C-E; Fig EV2A-D) in $HeLa^{HexaKO}$, prompted us to analyze MIL^+ profiles using CD63 as a previously published marker for amphisomes (Oe *et al*, 2022). We found a 3.2-fold increase in overlap between MIL^+ and $CD63^+$ profiles in $HeLa^{HexaKO}$ relative to $HeLa^{WT}$ (Fig EV3A-C). Although membranes were not well preserved due to permeabilization, we observed by correlative light electron microscopy MPL^+ profiles in $HeLa^{WT}$ cells that had a morphology consistent with degradative

compartments, i.e. autolysosomal or late endolysosomal in nature (Appendix Fig S2A,B). MIL^+ fluorescence in $HeLa^{HexaKO}$ overlapped with structures that appeared as amphisomes/late endosomes (Appendix Fig S2C,D). The staining with MIL or MPL is informative concerning the state of membranes associated with the respective profiles (permeant vs non-permeant).

Amphisomes are believed to be a product of autophagosomal fusion with early and late endosomes (Gordon & Seglen, 1988). This includes MVBs, which contain intraluminal 40-60 nm vesicles and are the perceived fusion partners in amphisome formation (Berg *et al.*, 1998; Eskelinen *et al.*, 2002; Liou *et al.*, 1997). A simultaneous increase in amphisomes with reduction in autolysosomes (Fig 1E) suggests a precursor-product relationship for amphisome vis-à-vis autolysosomes, and indicates that in the absence of mATG8s the autophagic intermediates are arrested at the amphisomal stage. Amphisomal morphology was consistent with previously reported images of autophagic structures accumulating in $HeLa^{HexaKO}$ and not maturing into autolysosomes (Nguyen *et al.*, 2016). An increase in amphisomes cannot be explained by differences in endocytosis (the $HeLa^{HexaKO}$ $HeLa^{WT}$ showed similar uptake of fluid phase endocytic tracer; Fig EV3D,E) or a possible increase in MVBs in $HeLa^{HexaKO}$ cells, since their number remained similar in $HeLa^{HexaKO}$ and $HeLa^{WT}$ cells (Fig 1E, and Fig EV2C,D).

By SR dSTORM analyses, we observed in $HeLa^{HexaKO}$ HT-LC3B cells a variety of profiles including phagophores and apparently closed vesicular/globular structures that were not sealed (Fig 1F and Fig EV4A-C; quantification in Fig EV4D), since they remained permeant to small molecules and were stained with MIL. In parallel experiments, by immuno-EM of $HeLa^{HexaKO}$ transfected with GFP-LC3A, we observed immunogold labeling (using two methods for pre-embedding and post-embedding) of GFP inside the amphisome-like structures (Appendix Fig S3A,B), indicating that the vesicular/globular structures in $HeLa^{HexaKO}$ harbor markers of autophagosomes internally. Thus, we conclude that whereas autophagic organelles progress to the morphological stage known as amphisomes, the fine integrity of their membranes, reflected in permeability to small molecules exchanging with the cytosol, is compromised in the absence of mATG8s.

In vitro system for membrane sealing confirms the role of mATG8s

To further establish that mATG8s play a role in maintaining integrity of autophagosomal membranes we developed an in vitro assay termed SolVit (sealing of organellar limiting membranes in vitro) utilizing the HT-LC3B and MPL-MIL system as a reporter (Fig 2A). For SolVit, postnuclear supernatants (PNS) prepared by gentle sheer lysis of $HeLa^{HexaKO}$ cells stably expressing HT-LC3B (Acceptor) are combined with PNS from either $HeLa^{HexaKO}$ or $HeLa^{WT}$ lysates (Donor) in the presence or absence of ATP (to support biochemical reactions, including potential membrane repair/scission/expansion processes and mATG8 lipidation), followed by sequential staining with MIL and MPL. The resulting reaction products are then mounted in 96 well plates and subjected to HCM quantification of MPL^+ (red) and MIL^+ (green) profiles in up to 60 different fields

until a preset limit of 1,000 objects is reached (examples of fields presented in Fig 2B). Membrane sealing in vitro in ATP-dependent reactions, i.e. HT-LC3B sequestration and protection from covalent saturation by MIL, allows subsequent staining with MPL (Fig 2C). Addition of HeLa^{HexaKO} as donor PNS to the HeLa^{HexaKO} HT-LC3B acceptor PNS, yielded only an increase in MIL^{+} (unsealed) profiles and did not increase MPL^{+} (sealed) profiles (Fig 2Ci and ii). Addition of HeLa^{WT} PNS as donor to HeLa^{HexaKO} HT-LC3B as acceptor PNS, resulted in increased MPL^{+} (sealed) profiles (Fig 2Ci), also reflected in the MIL^{+}/MPL^{+} ratios (Fig 2Ciii). Thus, mATG8s are important for maintaining the integrity of LC3B+ positive organelles in vitro, confirming findings with whole-cell HCM studies.

Both GABARAP and LC3 subsets of mATG8s play a role in membrane sealing

We next tested whether both subfamilies, GABARPs and LC3s, play a role in keeping the LC3B^{+} profiles sealed. We derived HeLa lines stably expressing HT-LC3B (Fig 3A) in parental cells inactivated for three LC3s (LC3A,B,C; HeLa^{LC3TKO}) and three GABARAPs (GABARAP, L1, L2; HeLa^{GABATKO}) (Nguyen *et al.*, 2016), and subjected them to MPL-MIL HCM assay upon induction for autophagy by starvation in EBSS (Fig 3B and Fig EV 5A). Both HeLa^{LC3TKO} and HeLa^{GABATKO} cells displayed a decrease in sealed (MPL^{+}) profiles relative to HeLa^{WT} (Fig 3Bi) and increase in unsealed (MIL^{+}) HT-LC3B profiles (Fig 3Bii), similarly to HeLa^{HexaKO} cells (Fig 3Bi-iii). These relationships were refaced in MIL//MPL ratios (Fig 3Biii). As a further control, we treated cells induced for autophagy with BafA1 to block progression to degradative autolysosomes. As expected, EBSS induced MPL^{+} profiles in HeLa^{WT}, further increased in the presence of BafA1 (Fig 3Bi). The increase in MPL^{+} profiles with EBSS was diminished in HeLa^{HexaKO}, HeLa^{LC3TKO}, and HeLa^{GABATKO} cells and there was no detectable further MPL^{+} increase in the presence of BafA1 (Fig 3Bi). We transfected HeLa^{LC3TKO} with GFP-LC3A and HeLa^{GABATKO} cells with GFP-GABARAP (selected based on GST-pulldowns) and observed complementation by decreased MIL^{+} staining in cells expressing GFP-mATG8s fusion constructs (MPL could not be assessed due to fluorescence overlap between TMR and GFP) (Fig EV5B,C).

We additionally employed an independent, modified split luciferase-based assay to assess the accessibility of LC3B (Fig. EV5D). In the split-luciferase assay, NanoLuc holoenzyme is split into N-terminal HiBit 1.3-kDa domain and 18-kDa LgBit C-ter domain (Gremke *et al*, 2020). Cells (HeLa^{WT}, HeLa^{HexaKO}, HeLa^{LC3TKO} and HeLa^{GABATKO}) were transfected with the HiBit-LC3B expressing plasmid. They were then treated with the mTOR inhibitor PP242 to induce autophagy. Cells were subjected to PM permeabilization (using treatment as in the MPL-MIL HCM assay), after which LgBit was added along with the luciferase substrate furimazine in a non-lytic (membrane non-permeabilizing) buffer and luminescence quantified. Higher luciferase activity was observed in HeLa^{HexaKO}, HeLa^{LC3TKO} and HeLa^{GABATKO} relative to HeLa^{WT} (Fig. EV5D). This was indicative of increased access of LgBit to HiBit-LC3B localized within unsealed membranes. Further, autophagy receptors p62/SQSTM1, TAX1BP1 and NDP52 were protected from Proteinase K in a sequestrations/protease protection assay (Hasegawa *et al*, 2016; McEwan *et al*, 2015; Nguyen *et al.*, 2016; Shoemaker *et al*, 2019) more so

in HeLa^{WT} than in HeLa^{HexaKO} (Appendix Fig S4A-D). The results of the above assays are congruent and indicative of the role of both GABARAP and LC3 subsets as contributing to the sealing of autophagic membranes.

mATG8s GABARAP and LC3 subsets are required for proteolysis during autophagy

Recently, a new proteolytic assay was developed to reliably monitor autophagic flux in mammalian cells using HT-LC3B (Yim *et al*, 2022). In this test, termed HaloTag-based reporter processing assay, referred here as HaloTag^{TMR}-release assay (HTR), one monitors and quantifies the release of HaloTag covalently modified and thus stabilized with a compound containing haloalkane dehalogenase-reactive linker with tetramethylrhodamine (TMR; a fluorophore ligand used to reveal MPL^{+} autophagosomes). The released HaloTag^{TMR} is detectable and quantifiable in gels by TMR fluorescence or by Western blots and can be used to directly assess autophagic proteolysis employing HT-LC3B (Fig 3C,D). When we subjected to the HTR assay HeLa^{WT}, HeLa^{HexaKO}, HeLa^{LC3TKO}, and HeLa^{GABATKO} stably expressing HT-LC3B and induced for autophagy by starvation, only HeLa^{WT} cells displayed release of HaloTag^{TMR} quantified by in gel fluorescence and by immunoblotting (Fig 3C,D). During autophagy, HaloTag^{TMR} release increased with time (from 90 min to 6 h starvation) but only in HeLa^{WT} cells but not in HeLa^{HexaKO}, HeLa^{LC3TKO}, and HeLa^{GABATKO} backgrounds (Fig 3C,D). Using HTR assay and HaloTag^{TMR} release as a definitive reporter of proteolysis during autophagy (Yim *et al.*, 2022), our findings show that mATG8s and their GABARAP and LC3 subclasses are critical for the ability of autophagosomes to act as lytic organelles.

Subsets of mATG8s contribute to sealing of LC3B-positive membranes in vitro

We tested LC3s and GABARAPs subsets in the SolVit system (Fig 4A-D). For this, the acceptor PNS was from either HeLa^{LC3TKO} (Fig 4Aα) or HeLa^{GABATKO} (Fig 4Aβ) stably expressing HT-LC3B, combined with donor PNS preparations from HeLa^{WT}, HeLa^{LC3TKO} or HeLa^{GABATKO}. After incubation, the ATP-dependent products of the in vitro reaction were subjected to HCM quantification. When the acceptor was either HeLa^{LC3TKO} HT-LC3B or HeLa^{GABATKO} HT-LC3B, addition of cross-complementing PNS from HeLa^{WT} cells resulted in sealing of LC3B^{+} profiles in the presence of ATP reflected in increased MPL^{+} objects (Fig 4C,D panels i/red). A similar increase in MPL^{+} profiles was observed when heterologous PNS extracts were combined (HeLa^{LC3TKO} HT-LC3B x HeLa^{GABATKO} or HeLa^{GABATKO} HT-LC3B x HeLa^{LC3TKO}) but not when homologous PNS combinations were used (HeLa^{LC3TKO} HT-LC3B x HeLa^{LC3TKO} or HeLa^{GABATKO} HT-LC3B x HeLa^{GABATKO}) (Fig 4C,D). This was reflected in other parameters, e.g., MIL increased in products of homologous and decreased in products of heterologous reaction mixtures (Fig 4C,D, panels ii). Finally, MIL/MPL ratios increased in products of homologous and decreased in products of heterologous reaction mixtures (Fig 4C,D, panels iii). Thus, both GABARAP and LC3 members contribute to sealing of LC3B-positive membranes and maintaining them in a state impermeant to small molecules.

GABARAP and LC3A but not LC3B interact with ESCRT-I component VPS37A

To address mechanistically the type of activity that mATG8s provide to maintain autophagic membranes in a sealed state, we considered the possibility that mATG8s affect ESCRTs, a system known to play a role in general membrane maintenance upon damage or remodeling (Christ *et al.*, 2017; Hurley, 2015; Zhen *et al.*, 2021) and in autophagy during the final stages engaging ESCRT-I (Flower *et al.*, 2020; Takahashi *et al.*, 2019) and ESCRT-III components (Takahashi *et al.*, 2018; Zhen *et al.*, 2020). A component of the ESCRT-I complex, VPS37A, plays a key role in autophagosomal completion and is essential (Takahashi *et al.*, 2019) for autophagosomes to become sealed and inaccessible to small membrane-impermeant ligands (Flower *et al.*, 2020; Takahashi *et al.*, 2018). VPS37A encodes a ubiquitin E2 variant (UEV) domain (Bache *et al*, 2004), with the UEV in TSG101 known to bind ubiquitin (Pornillos *et al*, 2002). We hypothesized that mATG8s, which are ubiquitin-like molecules (Kumar *et al.*, 2021b; Mizushima, 2020), may interact with VPS37A. We hence tested whether mATG8s interacted with VPS37A. Direct interactions between VPS37A and several mATG8s from both LC3 and GABARAP subgroups were observed in GST pulldowns in vitro, with GABARAP and LC3A as standouts (Fig 5A). These interactions were confirmed by coimmunoprecipitations in cell extracts (Co-IP) (Fig 5B) and further details established in studies below. In conclusion, interaction experiments indicate that members of both subgroups of mATG8s, GABARAPs and LC3s, can bind VPS37A, with the notable exception of LC3B.

The N-terminal region of VPS37A interacts with mATG8s

AlphaFold modeling predicted that the N-terminal region of VPS37A (UniProt entry Q8NEZ2; https://alphafold.ebi.ac.uk/entry/Q8NEZ2) was disordered and that it interacted with mATG8s (Fig EV6A,B) with additional potential contacts elsewhere in VPS37A. We modeled interactions between mATG8s and VPS37A using $VPS37A^{deltaUEV}$ for reduced complexity and focused on the N-terminal region. Five independent iterative runs by AlphaFold yielded similar models ranked based on local Difference Distance Test (lDDT) confidence measure (Fig EV6C,D). In all 5 iterative models with either LC3A or GABARAP, the N-terminal residues of $VPS37A^{deltaUEV}$ were consistently predicted to interact with mATG8s (Fig EV6E,F). The rank 1 model (Fig 5C) was chosen as the representative model due to its highest confidence score for the N-terminus region of $VPS37A^{deltaUEV}$. It showed a predicted sidechain packing albeit with differences within the hydrophobic pocket of GABARAP and LC3A when compared to the known structure of LC3C in a complex with the PLEKHM1 (LC3-interacting region) LIR peptide (PDB DOI: 10.2210/pdb5DPW/pdb) (Rogov *et al*, 2017) (Fig EV6G - cyan PLEKHM1 LIR; green N-Ter VPS37A). Thus, AlphaFold predicts at least one binding site (the N-terminal region) within $VPS37A^{deltaUEV}$ for association with GABARAP and LC3A, albeit additional contacts elsewhere in the molecule are possible.

We compared three constructs: GST-$VPS37A^{FL}$ (full length, Fig 5D I), GST-$VPS37A^{deltaUEV}$ (UEV domain deleted from the construct, Fig 5D II), and GST-UEV^{VPS37A}

(only the UEV domain, Fig 5D III), with UEV being defined per the NCBI entry NP_689628.2. Unexpectedly, the GST-UEV^{VPS37A} protein did not associate with mATG8s whereas GST-VPS37A^{deltaUEV} did (Fig 5E), a surprising finding that was confirmed in Co-IPs with LC3A (Fig 5F). Previous work (Takahashi *et al.*, 2019) has presented evidence and concluded that the UEV domain of VPS37A was essential for autophagosomal closure. However, the constructs used in that study (VPS37A$^{deltaN(1-90)}$; also known as VPS37A variant 4, Fig 5D IV) had in addition to the missing portion of the UEV domain a deletion of the entire N-terminal region (residues 1-22; red in Fig 5D) (Takahashi *et al.*, 2019). We thus tested by Co-IPs whether the N-terminus of VPS37A binds to GABARAP and LC3A as predicted by AlphaFold. A deletion of the residues 1-90 (Fig 5D IV), which has been reported to abrogate VPS37A ability to guide autophagosomal closure (Takahashi *et al.*, 2019), resulted in a loss of interactions with LC3A and GABARAP expressed as GFP fusions (Fig 5G,H). An N-terminal deletion of the first 20 residues alone of VPS37A (Fig 5D V) abrogated interactions detectable by Co-IP (Fig 5G,H). Lastly, the N-terminus of VPS37A (aa 1-22, including a Gly-Gly motif after the first 20 residues; Fig EV5A) when fused to the N-terminus of GFP (Fig 5D VI) and FLAG at the N-terminus of VPS37A to perform Co-IPs, was able to bind GFP-LC3A and GFP-GABARAP (Fig 5G,H). Since the predicted binding site for VPS37A within mATG8s overlaps the LIR docking site (LDS; Fig EV6G), we did not further analyze this region by point mutations due to likely pleiotropic effects of changing LDS (Lamark & Johansen, 2021). In conclusion, the N-terminal region of the ESCRT I protein VPS37A associates with LC3A and GABARAP.

Interaction between mATG8s and VPS37A contributes to autophagosomal seal

We next confirmed that VPS37A KO affects membrane sealing using the MPL-MIL HCM assay, followed by complementation with mATG8s-binding and non-binding VPS37A constructs. Due to technical issues, we generated stable HT-LC3B transfectants in a different cell line, Huh7. Huh7 is a well-differentiated hepatocyte derived carcinoma cell line and its derivatives have been used as experimental substitute for primary hepatocytes. Huh7 have been extensively used in autophagy and mATG8s studies (Claude-Taupin *et al*, 2021; Gu *et al*, 2019; Jia *et al*, 2020a; Jia *et al*, 2020b; Jia *et al*, 2022; Kumar *et al.*, 2021a). First, we knocked down VPS37A in Huh7-HT-LC3B stable cells and quantified by MPL-MIL HCM assay autophagosomal permeability (Fig EV7A-B). In accordance with previous observations (Takahashi *et al.*, 2019), MPL^{+} profiles were diminished in Huh7-HT-LC3B cells knocked down for VPS37A (Fig EV7Ai), whereas MIL^{+} profiles as well as MIL/MPL ratios were increased (Fig EV7Aii,iii). We then knocked out VPS37A in this background to generate Huh7^{VPS37AKO} HT-LC3B cells. Due to fluorescence overlap between TMR and fluorescently labeled antibody used to gate on transfected cells we could assay only MIL whereas MPL could not be assessed. The increased MIL^{+} phenotype in Huh7^{VPS37AKO} HT-LC3B cells could be complemented with full length VPS37A (FLAG-VPS37A^{FL}) which binds mATG8s, but not with FLAG-VPS37A$^{deltaN(1-20)}$, which does not bind mATG8s (Fig 5I,J). This indicates that the interaction between mATG8s and VPS37A is critical for autophagosomal sealing.

The role of VPS37A binding to mATG8s was further tested in both proteinase K protection assay for p62 sequestration (Fig. EV8A-C) and in the HTR assay (Fig. EV8D-E). The effect of the loss of VPS37A in Huh7^{VPS37AKO} on p62 sequestration and protection from proteinase K in Huh7^{VPS37AKO} HT-LC3B cells was complemented by expression of FLAG-VPS37^{FL} but not by expression of FLAG-VPS37$^{deltaN(1-20)}$ (Fig. EV8A-C). Likewise, in the HTR assay, HaloTag^{TMR} release was observed in Huh7^{VPS37AKO} cells complemented with FLAG-VPS37^{FL} but not with FLAG-VPS37$^{deltaN(1-20)}$ or FLAG-VPS37$^{deltaN(1-90)}$ (Fig. EV8D,E).

The above findings indicate that mATG8s and VPS37A mechanistically work together in membrane maintenance and sealing of autophagosomal organelles.

ESCRTs maintain autophagosomal membrane imperviousness during mitophagy

As ESCRT-I components were tested above and elsewhere (Flower *et al.*, 2020) in sealing of autophagic membranes during starvation, we wanted to test their role in maintaining autophagosomal membranes during a different type of autophagy, i.e. Parkin-dependent mitophagy (Youle, 2019). However, we could not use HeLa cells expressing YFP-Parkin (Narendra *et al*, 2008; Nguyen *et al.*, 2016) in the MPL-MIL HCM assay due to the overlap between YFP-Parkin fluorescence and MPL. We thus employed Huh7 cells which express endogenous Parkin and responded to inducer of mitophagy CCCP by reduced bands of mitochondrial COX-II, previously used as a mitophagy readout (Nguyen *et al.*, 2016) (Fig EV7C). We knocked out individually VPS37A and VPS37B (Fig 6Ai,ii), both components of the ESCRT-I helical filaments important for autophagosome completion via membrane scission (Flower *et al.*, 2020). We found that both VPS37A and VPS37B were required to maintain autophagosomal membranes in a sealed state during mitophagy determined by the MPL-MIL HCM (Fig 6A-E). In either Huh7^{VPS37AKO} HT-LC3B or Huh7^{VPS37BKO} HT-LC3B cells, MIL^{+} profiles were increased relative to WT cells (Fig 6Bii,Dii). This MIL^{+} increase could not be attributed to p62-LC3B-I aggregates previously reported in cells under basal conditions when autophagosome biogenesis was blocked (Runwal *et al*, 2019), since there was no change in MIL^{+} puncta counts under basal conditions between WT and VPS37A KO cells (Fig EV7D). Regardless, in either Huh7^{VPS37AKO} HT-LC3B (Fig 6Bii) or Huh7^{VPS37BKO} HT-LC3B (Fig 6Dii), MPL^{+} profiles induced by CCCP treatment were diminished relative to Huh7^{WT} HT-LC3B cells (Fig 6Bi,Di), whereas MIL/MPL ratios were increased in Huh7^{VPS37AKO} HT-LC3B (Fig 6Biii) or Huh7^{VPS37BKO} HT-LC3B (Fig 6Diii). This shows that the number of autophagosomes impervious to the MIL ligand was reduced in VPS37A and VPS37B KO cells. Other parts of the ESCRT machinery were needed, since a knockdown of ESCRT-III component CHMP2A (Fig 6F-H), previously implicated in starvation-induced autophagy (Flower *et al.*, 2020; Takahashi *et al.*, 2018; Takahashi *et al.*, 2019), caused membrane permeability phenotype during mitophagy similar to the ESCRT-I components tested above.

The deletion of the N-terminal 20 residues from VPS37A (expressed as FLAG-VPS37A$^{deltaN(1-20)}$ compared to FLAG-VPS37A^{FL}) did not reduce its ability to form complexes with another partner within the ESCRT-I protomer (GFP-TSG101) (Appendix

Fig S5A,B). We postulate that its effects are instead at the recruitment of VPS37A to autophagosomes, although it may also influence supramolecular structures, such as ESCRT-I filaments (Flower *et al.*, 2020) (Appendix Fig S5C,D).

VPS37A and its ability to interact with mATG8s is required to maintain membrane imperviousness during mitophagy

We next wanted to establish whether VPS37A, the ESCRT-I protein interacting with mATG8s, plays an equivalent role during mitophagy as it does during starvation. We first tested in the SolVit assay whether VPS37A was important for rendering autophagosomes impervious to small molecules during mitophagy induced by CCCP. For in vitro complementation test, the acceptor PNS was from stable Huh7^{VPS37AKO} HT-LC3B cells combined with heterologous donor PNS from Huh7 WT or homologous donor PNS from Huh7^{VPS37AKO} HT-LC3B cells, both donor and acceptor treated with CCCP (Fig 7A). After incubation, the ATP-dependent products of the in vitro reaction were subjected to HCM quantification (Fig 7Bi-iii, and Fig EV7E). As in other SolVit experiments, addition of ATP stimulated slightly MIL^{+} profiles likely reflecting continuing ATP-dependent conjugation processes (Fig 7Bii). Addition of cross-complementing PNS from Huh7^{WT} cells resulted in sealing of LC3B^{+} profiles reflected in increased MPL^{+} objects (Fig 7Bi/red) but not when homologous combination was used containing PNS from VPS37A KO cells (Fig 7A,B). This was also reflected in MIL^{+} parameters (Fig 7Bii/green). Finally, MIL/MPL ratios increased after reactions between homologous PNS and decreased in heterologous PNS reactions (Fig 7Biii). Thus, in cells induced for mitophagy, VPS37A is important for maintaining autophagosomal membranes impermeant to small probes.

As with starvation-induced autophagy, interaction between VPS37A and mATG8s was important for integrity of autophagosomal membrane during mitophagy. The increased MIL^{+} phenotype in Huh7^{VPS37AKO} HT-LC3B cells was complemented (suppressed) by full length VPS37A (FLAG-VPS37A^{FL}) which binds mATG8s, but not with FLAG-VPS37A$^{deltaN(1-20)}$ or FLAG-VPS37A$^{deltaN(1-90)}$ (Fig 7C,D), neither one of which binds mATG8s (Fig 6G,H). This indicates that the interaction between mATG8s and VPS37A is critical for autophagosomal membrane impermeability during mitophagy, and that the mATG8s-ESCRT-I relationship is critical during membrane remodeling in diverse presentations of canonical autophagy.

Discussion

The experiments presented herein show that mATG8s interact with key ESCRT-I components orchestrating ESCRTs to maintain autophagosomal membranes in a sealed, nonporous state thus enabling autophagic intermediates to progress into lytic organelles. A model emerges in which mATG8s affect ESCRT-I component VPS37A, shown to be essential for sealing of the autophagosome (Takahashi *et al.*, 2019). The role of mATG8s in the maintenance of autophagic structures in an impervious state represents their key and previously unappreciated function and expands the portfolio of mATG8s' roles that include interactions with autophagic cargo receptors (Lamark & Johansen, 2021; Randow & Youle, 2014; Stolz *et al.*, 2014), membrane perturbation during canonical autophagosome formation (Maruyama *et al.*, 2021), a kinetic role in autophagosome-lysosome fusion (Tsuboyama *et al.*, 2016), and participation in non-canonical processes (Deretic & Lazarou, 2022).

In the absence of VPS37A, autophagic organelles have been reported to remain at more immature morphological stages, i.e. as phagophores and double membrane autophagosomes (Takahashi *et al.*, 2019). We did observe unclosed phagophores in hexa mATG8-KO cells by EM and SR microscopy although we did not detect by enumeration significant accumulation of early autophagic structures. These variances suggest that VPS37A is essential for closure whereas mATG8s act as facilitators potentially augmenting this process, akin to what has been reported for other kinetic effects of mATG8s (Tsuboyama *et al.*, 2016). In addition, mATG8s are necessary to maintain autophagic organelles in a sealed state, and in the absence of mATG8s the quality of the initial seal or the continuing membrane integrity are compromised. Other studies have shown that in the absence of the mATG8 lipidation machinery, which affects both LC3s and GABARAPs, there is accumulation of unclosed autophagosomes (Fujita *et al*, 2008; Itakura *et al*, 2012; Komatsu *et al*, 2005; Sou *et al*, 2008). More recent elegant studies have used autophagy receptors in protease protection assays as a probe for autophagosomal closure indicating that autophagic phagophores can close even in the absence of mATG8s (Nguyen *et al.*, 2016) or mATG8s' lipidation (Ohnstad *et al.*, 2020). These variances have been in part explained by the kinetic effects of mATG8s due to longer or shorter times of autophagy induction in different studies, which may be of relevance in our experiments. However, our principal finding that autophagosomal membranes are actively maintained in a sealed state lest they become permeant to molecules such as the MIL probe, indicate that even when morphologically appearing as closed, autophagosomal organelles can be permeant in the absence of mATG8s. This permeability is to small molecules such as HaloTag ligands, and to macromolecules based on permeability to the 18-kDa LgBit C-ter domain of the NanoLuc luciferase in the split luciferase assay.

The autophagic structures observed in our study in the absence of key ATG8s, are arrested at a stage morphologically equal to amphisomes, compatible with the ultrastructural images of autophagic profiles previously seen in mATG8s KO cells (Nguyen *et al.*, 2016). In both our work and in the study by Nguyen et al., (Nguyen *et al.*, 2016), such organelles do not progress to autolysosomes, indicating a deficiency

preventing their conversion into strong lytic compartments. We show here that in mATG8 KO cells (hexa, GABATKO or LC3TKO), amphisomes, identified as LC3B$^+$ CD63$^+$ profiles (visualized as MIL-HT-LC3B$^+$ CD63$^+$ in our study) (Oe *et al.*, 2022), display increased staining with MIL. Thus, amphisomes along with other LC3B-positive membranes are permeant to small molecules possibly due to pores remaining in the absence of efficient ESCRT-dependent closure or due to a continuing need to maintain membrane integrity via ESCRTs given that autophagosomes sequester cargo that may potentially and repeatedly compromise delimiting membranes.

The role of both LC3 and GABARAP subsets in maintaining the LC3B membranes in a sealed state is unexpected given that prior observations have indicated that GABARAPs are more important in progression to autolysosomes than LC3s (Weidberg *et al.*, 2010). Since GABARAP appears to be stronger than LC3A in binding to VPS37A, this too can be the consequence of kinetic/facilitator effects of mATG8s. GABARAPs have stronger effects than LC3s in mitophagy assays, albeit LC3A does show some activity (Nguyen *et al.*, 2016). It has also been proposed that GABARAPs but not LC3s affect progression to autolysosomes via tethering molecules involved in autophagosome-lysosome fusion (Nguyen *et al.*, 2016). Thus, the process of maintaining autophagosomal membrane integrity by both categories of mATG8s, i.e. GABARAPs and LC3s, affecting ability of autophagic organelles to degrade substrates definitively demonstrated here in the HTR-release assay, is separable and different from the effects on fusion events (Nguyen *et al.*, 2016).

The apparent porousness of autophagic membranes may be due to a single closure point, a patchwork of membranes that require multiple points of closure, or due to the previously unappreciated aspect that membranes once closed need to be maintained in a sealed state due to the stress of continuous membrane expansion or incidental cargo penetration. Our findings uncover a new function for mATG8s and in sealing the autophagosomal membranes and in maintaining them in a sealed state, which is cortical to carry out degradation of autophagic substrates. Since degradative autophagy plays a role in many diseases and normal physiology (Klionsky *et al.*, 2021; Mizushima & Levine, 2020), understanding how mATG8s affect the quality of autophagic membranes and their ability to become degradative organelles, is of fundamental and applied significance.

Acknowledgments
We thank K. Tangavelou, and S. Kumar for their contributions. Sajjad Khan was Fulbright Fellow, Nanoscience and Microsystems Engineering. This work was supported by NIH grants (R37AI042999 and R01AI111935) and a center grant (P20GM121176) to V.D.

Authors contributions
Conceptualization, R.J., V.D.; Formal Analysis, R.J., A.J., T.D., Y.H., E.L.E., V.D.; Investigation and Validation, R.J., A.J., E.H., M.A.P., Y.H., E.L.E., V.D.; Resources, V.D.; Writing – Original draft, R.J., V.D.; Writing – editing, E.L.E., F.R., G.T., T.D.; Visualization, R.J., S.K., K.L., E.L.E., V.D.; Supervision, T.R., V.D.; Project Administration, V.D.; Funding Acquisition V.D.

Declaration of Interests
The authors declare no competing interests.

Inclusion and ethics
All institutional inclusion and ethics policies were followed.

Materials and Methods

Cell culture
HEK 293T cells were obtained from ATCC. Huh7 cells were from Rocky Mountain Laboratory. HeLa^{WT}, HeLa^{HexaKO}, HeLa^{LC3TKO} HeLa^{GABATKO} cells were grown as mentioned previously (Nguyen *et al.*, 2016). Huh7^{VPS37BKO}HT-LC3B, HeLa^{HexaKO}HT-LC3B, HeLa^{LC3TKO}HT-LC3B, HeLa^{GABATKO}HT-LC3B, Huh7^{VPS37AKO}HT-LC3B cells and respective parental cells were grown in DMEM supplemented with 10% fetal bovine serum and antibiotics. For starvation-induced autophagy, cells were washed three times in PBS and incubated for 90 min in EBSS. For mitophagy, cells were incubated with 20 μM CCCP in full medium for 6 h.

Generation of HaloTag-LC3B (HT-LC3B) stable cell lines
HeLa^{WT}, HeLa^{HexaKO}, HeLa^{LC3TKO}, and HeLa^{GABATKO}, Huh7^{WT} cells were infected with Halo/hMAP1LC3B-lentivirus particles and after 48 h of infection cells were incubated with puromycin (2 μg/ml) for 1 week to select the HaloTag-HT-LC3B stable clones. Huh7-HT-LC3B cell were used to generate Huh7^{VPS37BKO}HT-LC3B, Huh7^{VPS37AKO}HT-LC3B with 400 μg of hygromycin.

Generation of CRISPR mutant cells
For VPS37B and VPS37A knock out cells, the lentiviral vector carrying both Cas9 enzyme and a gRNA targeting VPS37A and VPS37B CRISPR cells were generated for this study (CGGTATTGAAGCATCCACTG, GGAAACTGGCCCACATGCGA) were transfected into HEK293T cells together with the packaging plasmids psPAX2 and pCMV-VSV-G at the ratio of 5: 3: 2. Two days after transfection, the supernatant

containing lentiviruses was collected and used to infect HeLa or Huh7 cells. 48 h hours after infection, the cells were treated with puromycin (2 μg/ml) for one week to select knockout cells, $Huh7^{WT}$ and $Huh7^{VPS37BKO}$. The knockouts were confirmed by western blotting. For Huh7-HT-LC3B stable cell line, knockouts for VPS37A and VPS37B were generated with hygromycin (final concentration of 400 μg/ml).

Antibodies and reagents

The following antibodies and dilutions were used: Mouse anti-Flag (Sigma; F1804; 0.5 μg/ml for IP and 1:1,000 for WB); Rabbit anti-GFP (Abcam; ab290; 0.5 μg/ml for IP and 1:4,000 for WB); Mouse anti-DNA antibody (Progen; 61014; 1:300 for IF); Mouse anti-LC3 (MBL;152-3; 1:400 for IF); Rabbit anti-MTCO2 (Abcam; ab110258; 1:1000 for WB); Rabbit anti-LC3B (CST; 27755s; 1:1000 for WB); Rabbit anti-Parkin (Abcam; ab15954;1:500 for WB). Rabbit Anti-CD63 (Sigma Millipore, SAB4301607) Dynabeads Protein G (Thermo Fisher Scientific; 10003D, 50 μL/ml for IP). We also used the following reagents: Bafilomycin A1 (BafA1, InvivoGen; 13D02-MM); CCCP (Sigma, C2759), PP242 (Sigma, P0037), Lipofectamine 2000 (Thermo Scientific, 11668019); Lipofectamine RNAiMAX (Thermo Scientific, 13778150); Goat anti-mouse IRDye 680 (LI-COR, 925-68020); Goat anti-rabbit IRDye 800 (LI-COR, 926-32211); membrane impermeant ligand (MIL), HaloTag ligand Alexa Fluor 660 (Promega, G8471); membrane permeant ligand (MPL), HaloTag ligand TMR (Promega, G8251). Nano-Glo® HiBiT Extracellular Detection System (Promega, N2420), Triton® X-100 (OmniPur, 9410-OP), digitonin (Sigma Aldrich, D5628), saponin (Sigma, S4521-25G). DMEM (Gibco, #11995040), and Penicillin-Streptomycin (1,000U/ml; Gibco, #15140122). OptiMEM and EBSS medias from Life Technologies. Dextran, Texas Red™, 3000 MW, Neutral (Thermo Fisher Scientific, D3329)

Plasmids and siRNA transfection

pDest-FLAG-$VPS37A^{Full}$, pDest-FLAG-UEV^{VPS37A}, pDest-FLAG-$VPS37A^{deltaUEV}$, pDest-FLAG-$VPS37A^{deltaN(1-90)}$, pDest-FLAG-$VPS37A^{deltaN(1-20)}$, pDest-FLAG-$VPS37A^{Nter-EGFP}$, pDest-GFP-LC3A, pDest-GFP-LC3C, pDest-GFP-GABARAP, GST-LC3A, GST-LC3B, GTS-LC3C, GST-GABARAP-GST-GABRAP-L1, GST-GABARAP-L2, were first cloned into pDONR221 (Gateway Technology cloning vector, Thermo Scientific) using a BP cloning reaction and the expression vectors were then made by a LR cloning reaction (Gateway, Thermo Fisher) in (pDEST) destination vectors. Plasmid constructs were verified by DNA-sequencing (Genewiz). Plasmids were transfected using Lipofectamine 2000 (Thermo Fisher Scientific, #11668019).

Immunoblotting and co-immunoprecipitation assays

Immunoblotting and co-immunoprecipitation (Co-IP) were performed as described previously (Kumar *et al*, 2018). For Co-IP, 10cm dish cells were transfected with 12 μg of plasmids, wherever stated, and lysed in NP-40 buffer containing protease inhibitor cocktail (Roche, # 11697498001) and PMSF (Sigma, # 93482). Lysates were mixed with 5 μg antibody and incubated at 4 °C for overnight followed by incubation with Dynabeads protein G (Life Technologies) for 4 h, at 4 °C. Beads were washed three times with PBS and then boiled with SDS-PAGE buffer for analysis of interacting protein

by immunoblotting. Quantification was based on three or more biologically independent replicates.

GST pull-down Assay

Recombinant GST and GST-fusion proteins were produced in Escherichia coli SoluBL21_(Genlantis, #C700200) by inducing expression in overnight cultures with 50-75 µg/mL isopropyl β-D-1-thiogalactopyranoside (IPTG). Expressed proteins were purified by immobilization on Glutathione Sepharose 4 Fast Flow beads (GE Healthcare, #17-5132-01). For GST pull-down assays, myc-tagged proteins were in vitro translated and radiolabeled with [35S]-methionine using the TNT T7 Reticulocyte Lysate System (Promega, #l4610). Ten µL of *In vitro* translated proteins were precleared to reduce nonspecific binding with 10µL of empty Glutathione Sepharose beads in 100µL of NETN buffer (50 mM Tris pH 8.0, 150 mM NaCl, 1 mM EDTA, 0.5% NP-40) supplemented with cOmplete™ EDTA-free Protease Inhibitor Cocktail (Roche, #1183617001) for 30 min at 4 °C. This was followed by incubation with purified GST or GST-fusion proteins for 1-2 h at 4 °C. The mixture was washed 5 times with NETN buffer by centrifugation at 2,500g for 2 min followed by addition of 2x SDS gel-loading buffer (100 mM Tris pH 7.4, 4% SDS, 20% Glycerol, 0.2% Bromophenol blue and 200 mM dithiothreitol (DTT) (Sigma, #D0632) and heating for 10 min. The proteins were then resolved by SDS-PAGE and the gel stained with Coomassie Brilliant Blue R-250 Dye (Thermo Fisher Scientific, #20278) to visualize the GST and GST-fusion proteins. The gel was vacuum-dried and radioactive signal detected by Bioimaging analyzer BAS-5000 (Fujifilm).

MPL-MIL HCM assay for assessment of autophagic membrane sealing

HaloTag-LC3B stable cell lines were seeded in 96 well plate at the density of 8,000 cells/well. After 18-24 h cells were induced for autophagy (EBSS for 90 min) or mitophagy (20 µM CCCP for 6 h). After induction, cells were incubated with Membrane Impermeant Ligand (MIL: Alexa Fluor-660 $663_{Ex}/690_{Em}$, 1 µM, Promega, G8471) prepared in 1x MAS buffer (220 mM mannitol, 70 mM sucrose, 10 mM KH2PO4, 5 mM MgCl2, 2 mM HEPES, 1 mM EGTA, from Sigma) containing PMP (XF-PMP, Agilent; 102504-100, 1.5 nM for Huh7 and 4 nM for HeLa cells) at 37 °C for 15 min. Cells were washed twice with 1x PBS and fixed with 4% paraformaldehyde (PFA, Sigma) in PBS for 5 min at RT. Cells were again washed twice with 1x PBS and incubated with Membrane-Permeant Ligand (MPL: TMR 5µM, $555_{Ex}/585_{Em}$, Promega, G8251) for 30 min at RT. Cells were washed once with 1x PBS and stained with Hoechst 33342 (Thermo Scientific, H3570, 1:1000) for 10 min at RT. Cells were washed twice and plate was scanned by High Content Microscopy (HCM) for automated image acquisition and quantification, iDEV software (Thermo) in 96-well plates (Kumar *et al.*, 2019). 6 wells/ samples and 1000 objects in ≥60 fields were scanned.

SolVit - In vitro assay for autophagic membrane sealing

In vitro sealing of lipid bilayer (SolVit) was developed for HCM platform with modification from the previously described assay for in vitro fusion (Kumar *et al.*, 2021a; Matsui *et al*, 2018; Moreau *et al.*, 2011). For SolVit, $HeLa^{HexaKO}$ HT-LC3B, $HeLa^{WT}$ and $HeLa^{HexaKO}$ cells were seeded in 100 mM dish at the density of 8-10 x 10^5 cells/plate and incubated

for 18-24 h. Next day cells were induced for autophagy for 90 min with EBSS. Cells were harvested and homogenized with B1 buffer (20 mM HEPES-KOH, pH 7.2, 400 mM sucrose, and 1 mM EDTA). Homogenates were centrifuged at 12,000g for 30 min at 4 °C and post nuclear supernatant (PNS) containing $HeLa^{WT}$ or $HeLa^{HexaKO}$ (Donors) and $HeLa^{HexaKO}$ HT-LC3B (Acceptor) membranes were mixed for 60min in the presence or absence of ATP and ATP regenerative system at 37 °C . Control samples were left on ice. After ATP regeneration, the samples were stained with MIL for 15min at 37^0C. Samples were fixed with 2% paraformaldehyde in PBS for 15min and sequentially stained with MPL for 30 min. samples were centrifuged at 43,000g for 1 h at 4 °C . Supernatants were discarded and pellets were resuspended in 100 µl of mounting media+ 100 µl B1 buffer and dispensed in 96 well plates (40 µM/well, at least 5 wells per sample). The plates were centrifuged at 1000g for 10 min to allow settling down of the membranes to bottom of the plate. The plates were scanned in Cell Insight CX7 High-Content Screening (HCS) Platform (Thermo). A minimum of 10,000 objects were scanned per well and 5 wells were used for technical error. Three or more (n) biologically independent experiments were carried out and analyzed on different plates to derive means, standard errors, and statistical significance.

In vitro complementation in the SolVit assay

For observing in vitro complementation effect, the PNS was extracted from either $HeLa^{LC3TKO}$ or $HeLa^{GABATKO}$ cells stably expressing HT-LC3B (acceptor) and combined with donor PNS preparations from $HeLa^{WT}$, $HeLa^{LC3TKO}$ or $HeLa^{GABATKO}$ cells and incubated at 37 °C in in the presence or absence of ATP for 1 h. After incubation samples were incubated with MIL for 15 min at 37 °C . Samples were fixed with 2% of PFA for 10 min at RT and sequentially stained with MPL for 30 min at RT in dark. Samples were centrifuged at 43,000g for 1 h at 4 °C . Supernatants were discarded and pellets were resuspended in 100 µL of mounting media+ 100 µl B1 buffer and dispensed in 96 well plates (40 µM/well, at least 5 wells per sample). The plates were centrifuged at 1000g for 10 min to allow settling down of the membranes to bottom of the plate. The plates were scanned in Cell Insight CX7 High-Content Screening (HCS) Platform (Thermo). A minimum of 10,000 objects were scanned per well and 5 wells were used for analysis.

$HaloTag^{TMR}$ release (HTR) assay

For observing $Halo^{TMR}$ $HeLa^{WT}$, $HeLa^{HexaKO}$, $HeLa^{LC3TKO}$ or $HeLa^{GABATKO}$ stably expressing HT-LC3B cells were subjected to EBSS induced autophagy for 1.5 h or 6 h. At the end of the treatment live cells were exposed to ± TMR for 20-30 min. After TMR treatment cells were harvested and lysed with lysed in NP-40 buffer containing protease inhibitor cocktail (Roche, # 11697498001) and PMSF (Sigma, # 93482) and lysates were boiled with 1X sample buffer at 95 °C for 5 min. For each sample, 20 µg of protein was separated by SDS-PAGE and imagined with BioRad ChemiDoc MP Imaging System. For in-gel fluorescence imaging, the gel was immediately visualized with BioRad ChemiDoc MP Imaging System after SDS-PAGE. Band intensities were measured with Gel Analyzer in the open-source image processing software, Version 6.1.

Luciferase assay

HiBit is an 11 amino acid high affinity binding peptide which rapidly binds to Large Bit (LgBit) luciferase subunit (Promega, N2420). For luciferase assay, cells were seeded in 60 mm dish and incubated for 12-16 h. After incubation, cells were transfected with 8 μg LC3HiBit reporter plasmid in 8 μL of Lipofectamine 2000 and incubated overnight. Next day cells were treated with DMSO or 2 μM PP242 for 6 h, after incubation cells were incubated with Nano Glo non-Lytic substrate (1:50) along with LgBit protein (1:100) and 4 nM plasma membrane permeabilizer (PMP), substrate was mixed with equal volume of media in each well, reagents were added and equilibrated for 10 min at room temperature. Bio luminescence was measured by reading plate with luminometer (BioTek, Synergy hTx MultiMode, Microplate Reader, 19042612).

AlphaFold prediction

Using ColabFold: AlphaFold2 using MMseqs2, a recently developed machine-learning-based protein and protein complex structure prediction program with the sequence from UniProt entries, we modeled interactions between VPS37A (VPS37A^{deltaUEV}) with LC3A, and GABARAP, to determine the binding interactions between VPS37A^{deltaUEV} and each of the proteins respectively. The following protein sequences from UniProt (UniProt, 2010) were used: VPS37A (ID: Q8NEZ2), LC3A (ID: QH9H492) and GABARAP (ID: O95166). The VPS37A^{deltaUEV} sequence was generated by removing residues 23-217 (UEV domain). Within ColabFold, the MMseq2 (UniRef + Environmental) was chosen for MSA (multiple sequence alignment) and unpaired + paired was chosen as the pair mode. The complex structure predictions were performed using the multimer-v1 option. To probe the convergence of the ColabFold predictions, the predictions were run using 3, 24, and 48 recycles, where recycling means the prior model predictions are placed back into the model to further refine the structure (Roney & Ovchinnikov, 2022). Moreover, the comparison between the 24 and 48 recycles shows much lower values (all except one were below 1.5 Å). This demonstrates that the predictions are likely to have reached convergence upon running for 48 recycles. This information not only reveals that the proteins have their correct structure predicted but also provides insight to future ColabFold predictions that 48 recycles is optimal for these protein complexes to reach convergence of their predicted structures. The root-mean-square deviation (RMSD) and binding interface analysis were calculated using the software package Bio3D (Grant *et al*, 2006; Skjærven *et al*, 2014). ColabFold produces five models which are independently executed from the same set of inputs. The predictions are then re-ranked according to the predicted Local Distance Difference Test score (pLDDT) for each model. ColabFold produces an lDDT graph for each run, which shows all five ranked models and their predicted lDDT C_α score at each residue. The ranking corresponds to where rank 1 is the best model and rank 5 is the poorest model out of those produced.

Transmission electron microscopy

For transmission electron microscopy analysis, HeLa^{WT} and HeLa^{HexaKO} cells were grown in 6 well plates until they became semi-confluent. After 90 min of EBSS starvation, cells were fixed with 2% glutaraldehyde (EM grade) in 0.2 M HEPES, pH 7.4.

After 30 min, the cells were scraped under a small volume of fixative and transferred to 1.5 mL tubes to be spun at full speed for 10 min at room temperature to get a firm pellet. The pellets continued the fixation for up to 2 h. Cells were post-fixed in 1% OsO4, dehydrated in ethanol and embedded in Epon resin. Thin sections were cut using an ultramicrotome, collected onto electron microscopy cupper grids, and stained with uranyl acetate and lead citrate. In order to count autophagic organelles (autophagosomes/phagophores, autolysosomes, amphisomes, MVBs, late endosomes/lysosomes), 93 images of each sample were taken at primary magnification of 4000x, using uniform random sampling. The images were zoomed on computer screen. Autophagic compartments were counted, and the cytoplasmic area was estimated by point counting and exhibited as profiles per square µm (Eskelinen, 2008).

Immuno electron microscopy

For labeling with rabbit GFP antibody (Abcam; ab290, 1:500), two different protocols were used, pre-embedding and post-embedding immunoEM. For pre-embedding immunoEM, HeLa^{HexaKO} cells were grown in glass cover slips in 6 cm dishes until they became sub-confluent, and transfected with 8 µg of plasmid encoding GFP-LC3A overnight. The cells were starved for 90 min with EBSS. For pre-embedding, cells were fixed in PLP-fixative (2% formaldehyde – 0.01 M sodium periodate – 0.075M lysine – 0.037M Na-phosphate buffer, pH 7.4) for 2 h at RT. After washing in 0.1M Na-phosphate buffer, the cells were permeabilized in buffer A (0.01% saponin3/0.1% BSA/0.1 M Na-PO4), incubated in rabbit anti-GFP diluted in buffer A for 1 h at RT, and washed in buffer A. After incubation in the secondary antibody (goat anti-rabbit IgG coupled to 1.2 nm gold, Nanoprobes #2004 Nanogold®-Fab' Goat anti-Rabbit IgG) the cells were washed in buffer A and 0.1 M Na-phosphate buffer, fixed in 1% glutaraldehyde for 10 min, and quenched with 50 mM glycine in phosphate buffer. The 1.2 nm gold particles were then silver enhanced using HQ SILVER Enhancement kit (Nanoprobes, #2012) according to manufacturer's instructions, and the cells were then embedded in Epon and thin sectioned as described above.

For post-embedding, cells were fixed with 4% paraformaldehyde, 0.1% glutaraldehyde (EM grade) diluted in 0.1M HEPES buffer, pH 7.4, for 2 h at RT, scraped off the culture dish under the fixative, and pelleted. The pellets were washed in PBS and embedded in 10% gelatin in PBS. Small cubes were cut from the cell pellet, infiltrated in 15% PVP-1.7M sucrose in PBS, mounted on sample holders, and frozen in liquid nitrogen. Thin sections were cut at -110 C and picked up to Pioloform-carbon-coated nickel grids using 2.3 M sucrose in PBS. The sections were immunolabeled with rabbit anti-GFP and goat anti-rabbit IgG – 10 nm gold (British BioCell EM.GAR10), and embedded in a mixture of 1.5% methyl cellulose and 0.4% uranyl acetate. The sections were photographed using Jeol 1400Plus transmission electron microscope.

Correlative light-electron microscopy (CLEM)

For CLEM, HeLa^{WT} and HeLa^{HexaKO} cells were seeded on gridded Mattek glass bottom dishes (MatTek, Cat No P35G-1.5-14-CGRD). Cells were starved in EBSS for 90 min, fixed in 4% PFA-PBS for 3-5 min, and incubated with 1× MAS containing XF-PMP and MIL (1:1000) for 30 min followed by MPL for 30 min. Cells of interest were identified by correlating the grid, and three-dimensional images were obtained by confocal

microscopy before processing for electron microscopy. The cells were then firmly fixed for electron microscopy using 2% glutaraldehyde in 0.2 M HEP ES, pH 7 .4, The Matted grid was used to locate the cells of interest and the samples were thin sectioned at 70 nm thickness, picked up on single slot grids and imaged at 80 kV on a Jeol JEM-1400 Plus transmission electron microscope. Confocal optical sections and EM images were overlayed using the ec-CLEM plugin in Icy (https://icy.bioimageanalysis.org/), utilizing features visible in both phase contrast images and EM images as landmarks.

Super-resolution microscopy

Hela^{HexaKO} cells were plated on 25 mM coverslips in 6 well plate (Warner instruments) and allowed to attach for 12-18 h, by incubating at 37˚C, after incubation cells were starved in EBSS for 90 min. Cells were stained with MIL in presence of PMP for 15 min. After 15 min. The cells were washed with 1X PBS and then chemically fixed in two steps. The cells were first treated with 0.6% paraformaldehyde (PFA), 0.1% glutaraldehyde (GA), in PBS for 60 seconds. The cells were then fixed for 2-2.5 h in 3% PFA and 1% GA in PBS. The coverslip was mounted on Attofluor cell chamber with 1.5 mL of imaging buffer which consist of an enzymatic oxygen scavenging system and primary thiol: 50 mM Tris, 10 mM NaCl, 10% w/v glucose, 168.8 U/ml glucose oxidase (Sigma #G2133), 1404 U/ml catalase (Sigma #C9332), and 1 M 2-aminoethanethiol (MEA), pH 8.50. The sealed Attofluor chamber was placed at room temperature to allow the oxygen-scavenging reaction to progress for 30 minutes before the imaging. A custom-built sequential microscope controlled by custom written software (github.com/LidkeLab/matlab-instrument-control) in MATLAB (MathWorks Inc.) was used to perform dSTORM imaging. A high power 647 nm laser (2RU-VFL-P-500-647-B1R, MPB Communications) was used as an excitation laser and 405 nm diode laser (DL5146-101S, Thorlabs) was used to accelerate the dark to fluorescent state transition. A 100X silicon oil immersion objective (UPLSAPO100XS, Olympus) was used to collect emitted fluorescent light. 708/75 nm bandpass filter (FF01-708/75-25-D, Semrock) was placed in the emitted fluorescence light path. An sCMOS camera (C11440-22CU, Hamamatsu) was used to detect emitted fluorescence light. At first brightfield reference image was taken using 660 nm LED (M660L3, Thorlabs) illumination lamp and saved. During data acquisition, 15 sequences of 6,000 frames (a total of 90,000) were collected at 100 Hz. The saved brightfield reference image was used to realign each cell during second round of imaging. Data was analyzed via a 2D localization algorithm based on maximum likelihood estimation (MLE) (Huang *et al*, 2011; Smith *et al*, 2010). The low-quality and false localizations were filtered out by placing several thresholds on minimum number of detected photons, PSF width, localization error, and goodness of the fit of PSF model as defined by a p-value (Huang *et al.*, 2011). A frame connection algorithm (Wester, 2021 #17356) was applied to combine repeated localizations of the same emitter for the same blinking event. This is followed by drift correction algorithm (Wester *et al*, 2021) to correct for residual sample drift. The accepted emitters were used to reconstruct the Gaussian super-resolution images. Each accepted emitter was represented by a 2D Gaussian function with localization precisions (σ_x, σ_y) calculated from Cramér-Rao Lower Bounds (CRLB).

Statistical analysis

Statistical analysis was carried out using GraphPad Prism 9. For HCM, typical sample size was n=3-6 (biological replicates each on different pates). Technical replicates for HCM were typically six wells per condition, averaged to produce average value per plate per condition. For HCM, sample size was based on a historic (professional statistician) power analysis from prior studies, with large effect size (differences and variability/standard deviation from published studies), power 80%, β 20%, and α 5%, favoring type II errors (false negative) over type I errors (false positive), and assuming normal distribution. Band intensity in immunoblots, n=3 (biological replicates); no power analysis was performed. Data: means $\pm$ SD ($n \geq 3$). ANOVA and pot-hoc modified t-tests tests or t-test (two-tailed) were used. Statistical significance: $p<0.05$.

Data and materials availability

All primary data and unique materials (at a reasonable cost) are available on request from RJ and VD. Commercial or previously published materials are appropriately identified.

References

Axe EL, Walker SA, Manifava M, Chandra P, Roderick HL, Habermann A, Griffiths G, Ktistakis NT (2008) Autophagosome formation from membrane compartments enriched in phosphatidylinositol 3-phosphate and dynamically connected to the endoplasmic reticulum. *J Cell Biol* 182: 685-701

Bache KG, Slagsvold T, Cabezas A, Rosendal KR, Raiborg C, Stenmark H (2004) The growth-regulatory protein HCRP1/hVps37A is a subunit of mammalian ESCRT-I and mediates receptor down-regulation. *Mol Biol Cell* 15: 4337-4346

Berg TO, Fengsrud M, Stromhaug PE, Berg T, Seglen PO (1998) Isolation and characterization of rat liver amphisomes. Evidence for fusion of autophagosomes with both early and late endosomes. *J Biol Chem* 273: 21883-21892

Chang C, Jensen LE, Hurley JH (2021) Autophagosome biogenesis comes out of the black box. *Nat Cell Biol* 23: 450-456

Christ L, Raiborg C, Wenzel EM, Campsteijn C, Stenmark H (2017) Cellular Functions and Molecular Mechanisms of the ESCRT Membrane-Scission Machinery. *Trends Biochem Sci* 42: 42-56

Claude-Taupin A, Jia J, Bhujabal Z, Garfa-Traore M, Kumar S, da Silva GPD, Javed R, Gu Y, Allers L, Peters R *et al* (2021) ATG9A protects the plasma membrane from programmed and incidental permeabilization. *Nat Cell Biol* 23: 846-858

Deretic V (2021) Autophagy in inflammation, infection, and immunometabolism. *Immunity* 54: 437-453

Deretic V, Kroemer G (2021) Autophagy in metabolism and quality control: opposing, complementary or interlinked functions. *Autophagy* IN press: 1-10

Deretic V, Lazarou M (2022) A guide to membrane atg8ylation and autophagy with reflections on immunity. *J Cell Biol* 221

Dong S, Wang Q, Kao YR, Diaz A, Tasset I, Kaushik S, Thiruthuvanathan V, Zintiridou A, Nieves E, Dzieciatkowska M *et al* (2021) Chaperone-mediated autophagy sustains haematopoietic stem-cell function. *Nature* 591: 117-123

Eskelinen EL (2008) Fine structure of the autophagosome. *Methods Mol Biol* 445: 11-28

Eskelinen EL, Illert AL, Tanaka Y, Schwarzmann G, Blanz J, Von Figura K, Saftig P (2002) Role of LAMP-2 in lysosome biogenesis and autophagy. *Mol Biol Cell* 13: 3355-3368

Flower TG, Takahashi Y, Hudait A, Rose K, Tjahjono N, Pak AJ, Yokom AL, Liang X, Wang HG, Bouamr F *et al* (2020) A helical assembly of human ESCRT-I scaffolds reverse-topology membrane scission. *Nat Struct Mol Biol* 27: 570-580

Fujita N, Hayashi-Nishino M, Fukumoto H, Omori H, Yamamoto A, Noda T, Yoshimori T (2008) An Atg4B mutant hampers the lipidation of LC3 paralogues and causes defects in autophagosome closure. *Mol Biol Cell* 19: 4651-4659

Galluzzi L, Green DR (2019) Autophagy-Independent Functions of the Autophagy Machinery. *Cell* 177: 1682-1699

Ge L, Melville D, Zhang M, Schekman R (2013) The ER-Golgi intermediate compartment is a key membrane source for the LC3 lipidation step of autophagosome biogenesis. *Elife* 2: e00947

Ge L, Zhang M, Kenny SJ, Liu D, Maeda M, Saito K, Mathur A, Xu K, Schekman R (2017) Remodeling of ER-exit sites initiates a membrane supply pathway for autophagosome biogenesis. *EMBO Rep* 18: 1586-1603
Ge L, Zhang M, Schekman R (2014) Phosphatidylinositol 3-kinase and COPII generate LC3 lipidation vesicles from the ER-Golgi intermediate compartment. *Elife* 3: e04135
Ghanbarpour A, Valverde DP, Melia TJ, Reinisch KM (2021) A model for a partnership of lipid transfer proteins and scramblases in membrane expansion and organelle biogenesis. *Proc Natl Acad Sci U S A* 118
Goodwin JM, Walkup WGt, Hooper K, Li T, Kishi-Itakura C, Ng A, Lehmberg T, Jha A, Kommineni S, Fletcher K *et al* (2021) GABARAP sequesters the FLCN-FNIP tumor suppressor complex to couple autophagy with lysosomal biogenesis. *Sci Adv* 7: eabj2485
Gordon PB, Seglen PO (1988) Prelysosomal convergence of autophagic and endocytic pathways. *Biochem Biophys Res Commun* 151: 40-47
Grant BJ, Rodrigues AP, ElSawy KM, McCammon JA, Caves LS (2006) Bio3d: an R package for the comparative analysis of protein structures. *Bioinformatics* 22: 2695-2696
Gremke N, Polo P, Dort A, Schneikert J, Elmshauser S, Brehm C, Klingmuller U, Schmitt A, Reinhardt HC, Timofeev O *et al* (2020) mTOR-mediated cancer drug resistance suppresses autophagy and generates a druggable metabolic vulnerability. *Nat Commun* 11: 4684
Gu Y, Princely Abudu Y, Kumar S, Bissa B, Choi SW, Jia J, Lazarou M, Eskelinen EL, Johansen T, Deretic V (2019) Mammalian Atg8 proteins regulate lysosome and autolysosome biogenesis through SNAREs. *EMBO J* 38: e101994
Guo H, Chitiprolu M, Roncevic L, Javalet C, Hemming FJ, Trung MT, Meng L, Latreille E, Tanese de Souza C, McCulloch D *et al* (2017) Atg5 Disassociates the V1V0-ATPase to Promote Exosome Production and Tumor Metastasis Independent of Canonical Macroautophagy. *Dev Cell* 43: 716-730 e717
Hara T, Takamura A, Kishi C, Iemura S, Natsume T, Guan JL, Mizushima N (2008) FIP200, a ULK-interacting protein, is required for autophagosome formation in mammalian cells. *J Cell Biol* 181: 497-510
Hasegawa J, Iwamoto R, Otomo T, Nezu A, Hamasaki M, Yoshimori T (2016) Autophagosome-lysosome fusion in neurons requires INPP5E, a protein associated with Joubert syndrome. *EMBO J* 35: 1853-1867
Hayashi-Nishino M, Fujita N, Noda T, Yamaguchi A, Yoshimori T, Yamamoto A (2009) A subdomain of the endoplasmic reticulum forms a cradle for autophagosome formation. *Nat Cell Biol* 11: 1433-1437
He H, Dang Y, Dai F, Guo Z, Wu J, She X, Pei Y, Chen Y, Ling W, Wu C *et al* (2003) Post-translational modifications of three members of the human MAP1LC3 family and detection of a novel type of modification for MAP1LC3B. *J Biol Chem* 278: 29278-29287
Huang F, Schwartz SL, Byars JM, Lidke KA (2011) Simultaneous multiple-emitter fitting for single molecule super-resolution imaging. *Biomed Opt Express* 2: 1377-1393
Hurley JH (2015) ESCRTs are everywhere. *EMBO J* 34: 2398-2407
Ichimura Y, Kirisako T, Takao T, Satomi Y, Shimonishi Y, Ishihara N, Mizushima N, Tanida I, Kominami E, Ohsumi M *et al* (2000) A ubiquitin-like system mediates protein lipidation. *Nature* 408: 488-492

Itakura E, Kishi-Itakura C, Koyama-Honda I, Mizushima N (2012) Structures containing Atg9A and the ULK1 complex independently target depolarized mitochondria at initial stages of Parkin-mediated mitophagy. *Journal of cell science* 125: 1488-1499
Itakura E, Mizushima N (2010) Characterization of autophagosome formation site by a hierarchical analysis of mammalian Atg proteins. *Autophagy* 6
Itakura E, Mizushima N (2011) p62 Targeting to the autophagosome formation site requires self-oligomerization but not LC3 binding. *The Journal of cell biology* 192: 17-27
Jia J, Abudu YP, Claude-Taupin A, Gu Y, Kumar S, Choi SW, Peters R, Mudd MH, Allers L, Salemi M *et al* (2018) Galectins Control mTOR in Response to Endomembrane Damage. *Mol Cell* 70: 120-135 e128
Jia J, Bissa B, Brecht L, Allers L, Choi SW, Gu Y, Zbinden M, Burge MR, Timmins G, Hallows K *et al* (2020a) AMPK is activated during lysosomal damage via a galectin-ubiquitin signal transduction system. *Autophagy* 16: 1550-1552
Jia J, Claude-Taupin A, Gu Y, Choi SW, Peters R, Bissa B, Mudd MH, Allers L, Pallikkuth S, Lidke KA *et al* (2020b) Galectin-3 Coordinates a Cellular System for Lysosomal Repair and Removal. *Dev Cell* 52: 69-87 e68
Jia J, Wang F, Bhujabal Z, Peters R, Mudd M, Duque T, Allers L, Javed R, Salemi M, Behrends C *et al* (2022) Stress granules and mTOR are regulated by membrane atg8ylation during lysosomal damage. *J Cell Biol* 221
Kabeya Y, Mizushima N, Ueno T, Yamamoto A, Kirisako T, Noda T, Kominami E, Ohsumi Y, Yoshimori T (2000) LC3, a mammalian homologue of yeast Apg8p, is localized in autophagosome membranes after processing. *Embo J* 19: 5720-5728
Klionsky DJ, Petroni G, Amaravadi RK, Baehrecke EH, Ballabio A, Boya P, Bravo-San Pedro JM, Cadwell K, Cecconi F, Choi AMK *et al* (2021) Autophagy in major human diseases. *EMBO J* 40: e108863
Knaevelsrud H, Soreng K, Raiborg C, Haberg K, Rasmuson F, Brech A, Liestol K, Rusten TE, Stenmark H, Neufeld TP *et al* (2013) Membrane remodeling by the PX-BAR protein SNX18 promotes autophagosome formation. *J Cell Biol* 202: 331-349
Knorr RL, Lipowsky R, Dimova R (2015) Autophagosome closure requires membrane scission. *Autophagy* 11: 2134-2137
Komatsu M, Waguri S, Ueno T, Iwata J, Murata S, Tanida I, Ezaki J, Mizushima N, Ohsumi Y, Uchiyama Y *et al* (2005) Impairment of starvation-induced and constitutive autophagy in Atg7-deficient mice. *J Cell Biol* 169: 425-434
Kumar S, Gu Y, Abudu YP, Bruun JA, Jain A, Farzam F, Mudd M, Anonsen JH, Rusten TE, Kasof G *et al* (2019) Phosphorylation of Syntaxin 17 by TBK1 Controls Autophagy Initiation. *Dev Cell*
Kumar S, Jain A, Choi SW, da Silva GPD, Allers L, Mudd MH, Peters RS, Anonsen JH, Rusten TE, Lazarou M *et al* (2020) Mammalian Atg8 proteins and the autophagy factor IRGM control mTOR and TFEB at a regulatory node critical for responses to pathogens. *Nat Cell Biol* 22: 973-985
Kumar S, Jain A, Farzam F, Jia J, Gu Y, Choi SW, Mudd MH, Claude-Taupin A, Wester MJ, Lidke KA *et al* (2018) Mechanism of Stx17 recruitment to autophagosomes via IRGM and mammalian Atg8 proteins. *J Cell Biol* 217: 997-1013
Kumar S, Javed R, Mudd M, Pallikkuth S, Lidke KA, Jain A, Tangavelou K, Gudmundsson SR, Ye C, Rusten TE *et al* (2021a) Mammalian hybrid pre-

autophagosomal structure HyPAS generates autophagosomes. *Cell* 184: 5950-5969 e5922
Kumar S, Jia J, Deretic V (2021b) Atg8ylation as a general membrane stress and remodeling response. *Cell Stress* 5: 128-142
Lahiri V, Hawkins WD, Klionsky DJ (2019) Watch What You (Self-) Eat: Autophagic Mechanisms that Modulate Metabolism. *Cell Metab* 29: 803-826
Lamark T, Johansen T (2021) Mechanisms of Selective Autophagy. *Annu Rev Cell Dev Biol* 37: 143-169
Lee C, Lamech L, Johns E, Overholtzer M (2020) Selective Lysosome Membrane Turnover Is Induced by Nutrient Starvation. *Dev Cell* 55: 289-297 e284
Leidal AM, Huang HH, Marsh T, Solvik T, Zhang D, Ye J, Kai F, Goldsmith J, Liu JY, Huang YH *et al* (2020) The LC3-conjugation machinery specifies the loading of RNA-binding proteins into extracellular vesicles. *Nat Cell Biol* 22: 187-199
Levine B, Kroemer G (2019) Biological Functions of Autophagy Genes: A Disease Perspective. *Cell* 176: 11-42
Liou W, Geuze HJ, Geelen MJ, Slot JW (1997) The autophagic and endocytic pathways converge at the nascent autophagic vacuoles. *J Cell Biol* 136: 61-70
Loi M, Raimondi A, Morone D, Molinari M (2019) ESCRT-III-driven piecemeal micro-ER-phagy remodels the ER during recovery from ER stress. *Nat Commun* 10: 5058
Longatti A, Lamb CA, Razi M, Yoshimura S, Barr FA, Tooze SA (2012) TBC1D14 regulates autophagosome formation via Rab11- and ULK1-positive recycling endosomes. *J Cell Biol* 197: 659-675
Maeda S, Yamamoto H, Kinch LN, Garza CM, Takahashi S, Otomo C, Grishin NV, Forli S, Mizushima N, Otomo T (2020) Structure, lipid scrambling activity and role in autophagosome formation of ATG9A. *Nat Struct Mol Biol* 27: 1194-1201
Maruyama T, Alam JM, Fukuda T, Kageyama S, Kirisako H, Ishii Y, Shimada I, Ohsumi Y, Komatsu M, Kanki T *et al* (2021) Membrane perturbation by lipidated Atg8 underlies autophagosome biogenesis. *Nat Struct Mol Biol* 28: 583-593
Matoba K, Kotani T, Tsutsumi A, Tsuji T, Mori T, Noshiro D, Sugita Y, Nomura N, Iwata S, Ohsumi Y *et al* (2020) Atg9 is a lipid scramblase that mediates autophagosomal membrane expansion. *Nat Struct Mol Biol* 27: 1185-1193
Matsui T, Jiang P, Nakano S, Sakamaki Y, Yamamoto H, Mizushima N (2018) Autophagosomal YKT6 is required for fusion with lysosomes independently of syntaxin 17. *J Cell Biol*
McEwan DG, Popovic D, Gubas A, Terawaki S, Suzuki H, Stadel D, Coxon FP, Miranda de Stegmann D, Bhogaraju S, Maddi K *et al* (2015) PLEKHM1 regulates autophagosome-lysosome fusion through HOPS complex and LC3/GABARAP proteins. *Mol Cell* 57: 39-54
Mizushima N (2020) The ATG conjugation systems in autophagy. *Curr Opin Cell Biol* 63: 1-10
Mizushima N, Levine B (2020) Autophagy in Human Diseases. *N Engl J Med* 383: 1564-1576
Mizushima N, Levine B, Cuervo AM, Klionsky DJ (2008) Autophagy fights disease through cellular self-digestion. *Nature* 451: 1069-1075

Mizushima N, Noda T, Yoshimori T, Tanaka Y, Ishii T, George MD, Klionsky DJ, Ohsumi M, Ohsumi Y (1998) A protein conjugation system essential for autophagy. *Nature* 395: 395-398
Mizushima N, Yoshimori T, Ohsumi Y (2011) The role of Atg proteins in autophagosome formation. *Annu Rev Cell Dev Biol* 27: 107-132
Moreau K, Ravikumar B, Renna M, Puri C, Rubinsztein DC (2011) Autophagosome precursor maturation requires homotypic fusion. *Cell* 146: 303-317
Morishita H, Mizushima N (2019) Diverse Cellular Roles of Autophagy. *Annu Rev Cell Dev Biol* 35: 453-475
Nakamura S, Shigeyama S, Minami S, Shima T, Akayama S, Matsuda T, Esposito A, Napolitano G, Kuma A, Namba-Hamano T *et al* (2020) LC3 lipidation is essential for TFEB activation during the lysosomal damage response to kidney injury. *Nat Cell Biol* 22: 1252-1263
Narendra D, Tanaka A, Suen DF, Youle RJ (2008) Parkin is recruited selectively to impaired mitochondria and promotes their autophagy. *J Cell Biol* 183: 795-803
Nguyen TN, Padman BS, Usher J, Oorschot V, Ramm G, Lazarou M (2016) Atg8 family LC3/GABARAP proteins are crucial for autophagosome-lysosome fusion but not autophagosome formation during PINK1/Parkin mitophagy and starvation. *J Cell Biol* 215: 857-874
Nguyen TN, Padman BS, Zellner S, Khuu G, Uoselis L, Lam WK, Skulsuppaisarn M, Lindblom RS, Watts EM, Behrends C (2021) ATG4 family proteins drive phagophore growth independently of the LC3/GABARAP lipidation system. *Molecular Cell* 81: 2013-2030. e2019
Nishimura T, Tamura N, Kono N, Shimanaka Y, Arai H, Yamamoto H, Mizushima N (2017) Autophagosome formation is initiated at phosphatidylinositol synthase-enriched ER subdomains. *EMBO J* 36: 1719-1735
Oe Y, Kakuda K, Yoshimura SI, Hara N, Hasegawa J, Terawaki S, Kimura Y, Ikenaka K, Suetsugu S, Mochizuki H *et al* (2022) PACSIN1 is indispensable for amphisome-lysosome fusion during basal autophagy and subsets of selective autophagy. *PLoS Genet* 18: e1010264
Ohnstad AE, Delgado JM, North BJ, Nasa I, Kettenbach AN, Schultz SW, Shoemaker CJ (2020) Receptor-mediated clustering of FIP200 bypasses the role of LC3 lipidation in autophagy. *EMBO J* 39: e104948
Pornillos O, Alam SL, Rich RL, Myszka DG, Davis DR, Sundquist WI (2002) Structure and functional interactions of the Tsg101 UEV domain. *Embo J* 21: 2397-2406
Puri C, Renna M, Bento CF, Moreau K, Rubinsztein DC (2013) Diverse autophagosome membrane sources coalesce in recycling endosomes. *Cell* 154: 1285-1299
Puri C, Vicinanza M, Ashkenazi A, Gratian MJ, Zhang Q, Bento CF, Renna M, Menzies FM, Rubinsztein DC (2018) The RAB11A-Positive Compartment Is a Primary Platform for Autophagosome Assembly Mediated by WIPI2 Recognition of PI3P-RAB11A. *Dev Cell* 45: 114-131 e118
Randow F, Youle RJ (2014) Self and nonself: how autophagy targets mitochondria and bacteria. *Cell Host Microbe* 15: 403-411
Ravikumar B, Moreau K, Jahreiss L, Puri C, Rubinsztein DC (2010) Plasma membrane contributes to the formation of pre-autophagosomal structures. *Nat Cell Biol* 12: 747-757

Rogov VV, Stolz A, Ravichandran AC, Rios-Szwed DO, Suzuki H, Kniss A, Lohr F, Wakatsuki S, Dotsch V, Dikic I *et al* (2017) Structural and functional analysis of the GABARAP interaction motif (GIM). *EMBO Rep* 18: 1382-1396
Roney JP, Ovchinnikov S (2022) State-of-the-Art Estimation of Protein Model Accuracy using AlphaFold. *bioRxiv*
Runwal G, Stamatakou E, Siddiqi FH, Puri C, Zhu Y, Rubinsztein DC (2019) LC3-positive structures are prominent in autophagy-deficient cells. *Sci Rep* 9: 10147
Sanjuan MA, Dillon CP, Tait SW, Moshiach S, Dorsey F, Connell S, Komatsu M, Tanaka K, Cleveland JL, Withoff S *et al* (2007) Toll-like receptor signalling in macrophages links the autophagy pathway to phagocytosis. *Nature* 450: 1253-1257
Shoemaker CJ, Huang TQ, Weir NR, Polyakov N, Schultz SW, Denic V (2019) CRISPR screening using an expanded toolkit of autophagy reporters identifies TMEM41B as a novel autophagy factor. *PLoS Biol* 17: e2007044
Skjærven L, Yao X-Q, Scarabelli G, Grant BJ (2014) Integrating protein structural dynamics and evolutionary analysis with Bio3D. *BMC bioinformatics* 15: 1-11
Smith CS, Joseph N, Rieger B, Lidke KA (2010) Fast, single-molecule localization that achieves theoretically minimum uncertainty. *Nat Methods* 7: 373-375
Soreng K, Munson MJ, Lamb CA, Bjorndal GT, Pankiv S, Carlsson SR, Tooze SA, Simonsen A (2018) SNX18 regulates ATG9A trafficking from recycling endosomes by recruiting Dynamin-2. *EMBO Rep*
Sou YS, Waguri S, Iwata J, Ueno T, Fujimura T, Hara T, Sawada N, Yamada A, Mizushima N, Uchiyama Y *et al* (2008) The Atg8 conjugation system is indispensable for proper development of autophagic isolation membranes in mice. *Mol Biol Cell* 19: 4762-4775
Stolz A, Ernst A, Dikic I (2014) Cargo recognition and trafficking in selective autophagy. *Nat Cell Biol* 16: 495-501
Takahashi Y, He H, Tang Z, Hattori T, Liu Y, Young MM, Serfass JM, Chen L, Gebru M, Chen C *et al* (2018) An autophagy assay reveals the ESCRT-III component CHMP2A as a regulator of phagophore closure. *Nat Commun* 9: 2855
Takahashi Y, Liang X, Hattori T, Tang Z, He H, Chen H, Liu X, Abraham T, Imamura-Kawasawa Y, Buchkovich NJ *et al* (2019) VPS37A directs ESCRT recruitment for phagophore closure. *J Cell Biol* 218: 3336-3354
Tooze SA, Yoshimori T (2010) The origin of the autophagosomal membrane. *Nat Cell Biol* 12: 831-835
Tsuboyama K, Koyama-Honda I, Sakamaki Y, Koike M, Morishita H, Mizushima N (2016) The ATG conjugation systems are important for degradation of the inner autophagosomal membrane. *Science* 354: 1036-1041
Ulferts R, Marcassa E, Timimi L, Lee LC, Daley A, Montaner B, Turner SD, Florey O, Baillie JK, Beale R (2021) Subtractive CRISPR screen identifies the ATG16L1/vacuolar ATPase axis as required for non-canonical LC3 lipidation. *Cell Rep* 37: 109899
UniProt C (2010) The Universal Protein Resource (UniProt) in 2010. *Nucleic Acids Res* 38: D142-148
Valverde DP, Yu S, Boggavarapu V, Kumar N, Lees JA, Walz T, Reinisch KM, Melia TJ (2019) ATG2 transports lipids to promote autophagosome biogenesis. *J Cell Biol* 218: 1787-1798

Weidberg H, Shpilka T, Shvets E, Abada A, Shimron F, Elazar Z (2011) LC3 and GATE-16 N termini mediate membrane fusion processes required for autophagosome biogenesis. *Developmental cell* 20: 444-454
Weidberg H, Shvets E, Shpilka T, Shimron F, Shinder V, Elazar Z (2010) LC3 and GATE-16/GABARAP subfamilies are both essential yet act differently in autophagosome biogenesis. *The EMBO journal* 29: 1792-1802
Wester MJ, Schodt DJ, Mazloom-Farsibaf H, Fazel M, Pallikkuth S, Lidke KA (2021) Robust, fiducial-free drift correction for super-resolution imaging. *Sci Rep* 11: 23672
Xin Y, Yu L, Chen Z, Zheng L, Fu Q, Jiang J, Zhang P, Gong R, Zhao S (2001) Cloning, expression patterns, and chromosome localization of three human and two mouse homologues of GABA(A) receptor-associated protein. *Genomics* 74: 408-413
Yim WW, Yamamoto H, Mizushima N (2022) A pulse-chasable reporter processing assay for mammalian autophagic flux with HaloTag. *Elife* 11
Youle RJ (2019) Mitochondria-Striking a balance between host and endosymbiont. *Science* 365
Zhao YG, Zhang H (2019) Autophagosome maturation: An epic journey from the ER to lysosomes. *J Cell Biol* 218: 757-770
Zhen Y, Radulovic M, Vietri M, Stenmark H (2021) Sealing holes in cellular membranes. *EMBO J* 40: e106922
Zhen Y, Spangenberg H, Munson MJ, Brech A, Schink KO, Tan KW, Sorensen V, Wenzel EM, Radulovic M, Engedal N *et al* (2020) ESCRT-mediated phagophore sealing during mitophagy. *Autophagy* 16: 826-841

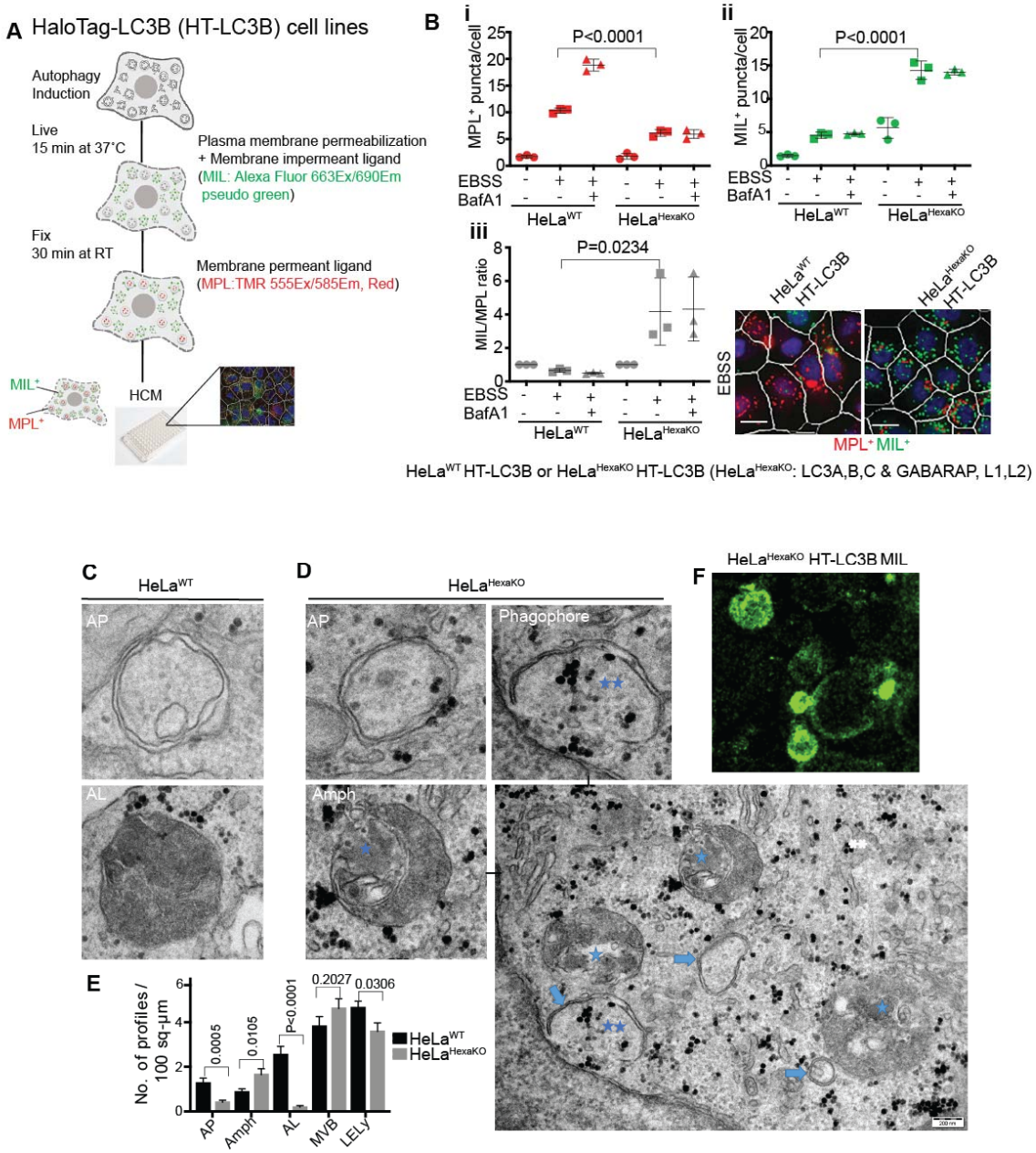

Figure 1. Mammalian ATG8s affect autophagosomal membrane permeability.

(A) Schematic representation of the MPL-MIL HCM assay: HaloTag based HT-LC3B MPL-MIL staining adapted for quantitative high content microscopy (HCM). MPL^+ profiles, HT-LC3B remaining available (not saturated with MIL during the preceding MIL staining step) to membrane permeant ligand. MIL^+ profiles, HT-LC3B accessible to membrane impermeant ligand.
(B) MPL-MIL HCM assay in $HeLa^{WT}$ and $HeLa^{HexaKO}$ expressing HT-LC3B, starved in EBSS for 90min ± 100 nM BafA1. Cells were sequentially incubated with HT ligands MIL and MPL, and HCM quantification carried out. Plasma membrane permeabilization

was carried out with 4 nM Agilent XF Plasma Membrane Permeabilizer/PMP. PMP was used during the MIL staining and prior to fixation in 4% paraformaldehyde. MPL staining followed the fixation. (B i) MPL-accessible membrane-bound HT-LC3B (remaining available to MPL after MIL saturation). (B ii) MIL-accessible membrane-bound HT-LC3B; (B iii) MIL/MPL puncta ratio. Circles, control samples (full medium); rectangles (EBSS); triangles (EBSS+BafA1); green, MIL; red, MPL; gray, MIL/MPL ratios. Images and statistics, HCM images (masks: white, primary objects/cells; red, MPL profiles; green, MIL profiles), one of 60 fields/well, 1,000 primary objects (cells) per well; 6 wells per plate (sampling error), triplicate plates (independent biological replicates). Statistical significance was determined by one-way ANOVA followed by Tukey's multiple comparison test. All values are mean ± SD, n = 3 biologically independent replicates.
(C-E) Selected electron microscopy (EM) images of $HeLa^{WT}$ and $HeLa^{HexaKO}$ EBSS-induced for autophagy for 90 min and their quantification (graph in F). AP, autophagosomes (phagophores or double membrane autophagosomes with content of similar electron-density to surrounding cytosol); Amph, amphisomes; AL, autolysosomes; MVB, multivesicular bodies; LELy, late endosomes or lysosomes. Statistics, unpaired t-test, two groups: $HeLa^{WT}$ and $HeLa^{HexaKO}$ (93 images each; sample mean, SE). Blue single asterisk, cytoplasmic cargo inside amphisome or autolysosome; double asterisk, phagophore structures; arrows, phagophores or autophagosomes.
(F) Super-resolution (dSTORM) of $HeLa^{HexaKO}$ HT-LC3B stained with MIL (note staining of the interiors of the globular structures).

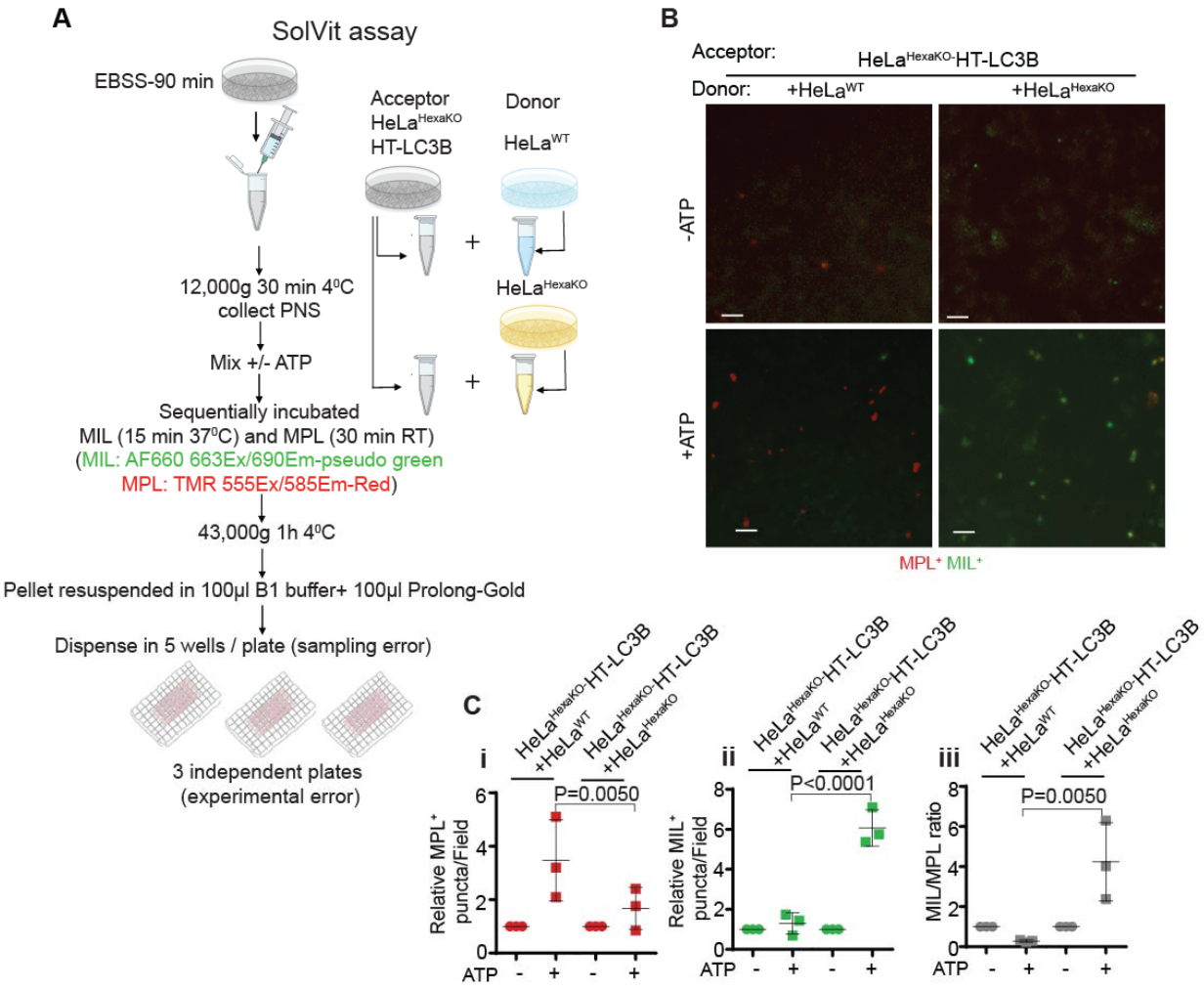

Figure 2. mATG8s direct the sealing of autophagosomal membranes in vitro.

(A) Representation of SolVit (sealing of organellar limiting membranes in vitro). Left (general schematic), cells serving as sources of donor or acceptor post nuclear supernatant (PNS) are starved in EBSS for 90 min, extracts prepared via repeat passages through a needle, and PNS collected after centrifugation at 12,000g. Upon incubation, reaction products are pelleted, resuspended and mounted in Prolong-Gold in 96-well plates for HCM. Right, acceptor PNS, $HeLa^{HexaKO}$ HT-LC3B ($HeLa^{HexaKO}$ cells stably expressing HT-LC3B) was incubated with donor PNS ($HeLa^{WT}$ or $HeLa^{HexaKO}$) ± ATP for 1 h, stained with MIL, fixed with 4% PFA, super-stained with MPL, and processed for HCM.
(B) Representative images of SolVit assay with $HeLa^{WT}$ and $HeLa^{HexaKO}$ as donors, and $HeLa^{HexaKO}$ HT-LC3B as acceptor. SolVit HCM images (example). MPL^+ (red), sealed $LC3B^+$ membranes MIL^+ (green), unsealed LCB^+ membranes;
(C) Quantification of MPL^+ and MIL^+ profiles (60 fields/well acquired): (C i) MPL^+ (red) puncta per field. (C ii) MIL^+ (green) puncta per field. (C iii) MIL^+/MPL^+ profile ratios (gray). Statistical significance was determined by one-way ANOVA followed by Tukey's multiple comparison test. All values are mean ± SD, n = 3 biologically independent

replicates, each HCM experiment: 1,000 valid primary objects/cells per well (max fields per well, 60), 5 wells/sample, Scale bar: 3 μm.

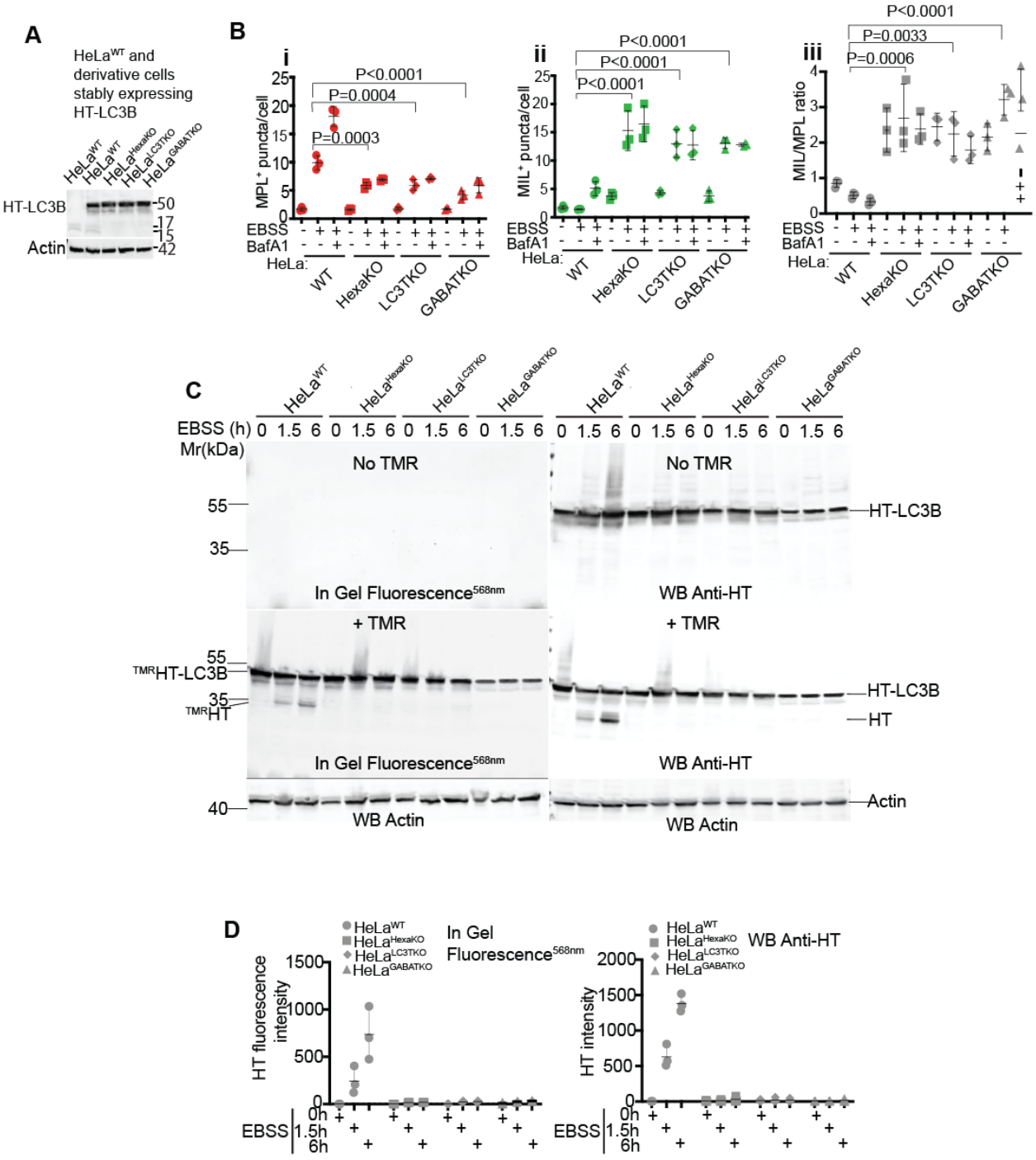

Figure 3. mATG8 subsets maintain autophagosomal membrane integrity and lytic capacity

(A) Western blot, Hela^{WT}, HeLa^{HexaKO}, HeLa^{LC3TKO}, HeLa^{GABATKO} stably expressing HT-LC3B.

(B) Cells were starved in EBSS for 90 min ±100 nM BafA1, sequentially incubated with MIL and MPL. MPL (B i; red), marker of sealed membranes; MIL (B ii; green), marker of unsealed membranes; profiles quantified by HCM. (B iii) MIL^{+}/MPL^{+} puncta ratio (gray),
(C) $Hela^{WT}$, $HeLa^{HexaKO}$, $HeLa^{LC3TKO}$, $HeLa^{GABATKO}$ stably expressing HT-LC3B were starved with EBSS for 90min or 6h. Cell were incubated with ± HaloTag ligand fluorescently labeled with TMR. In-gel fluoresce (TMR) and Western blots (anti-HaloTag antibody) of freed $HaloTag^{TMR}$ were imaged and band intensity quantified.
(D) Quantification of in-gel fluorescence band intensity and Western blot with anti-Halo antibody. Data, mean arbitrary intensity units; n=3 (independent biological replicates).

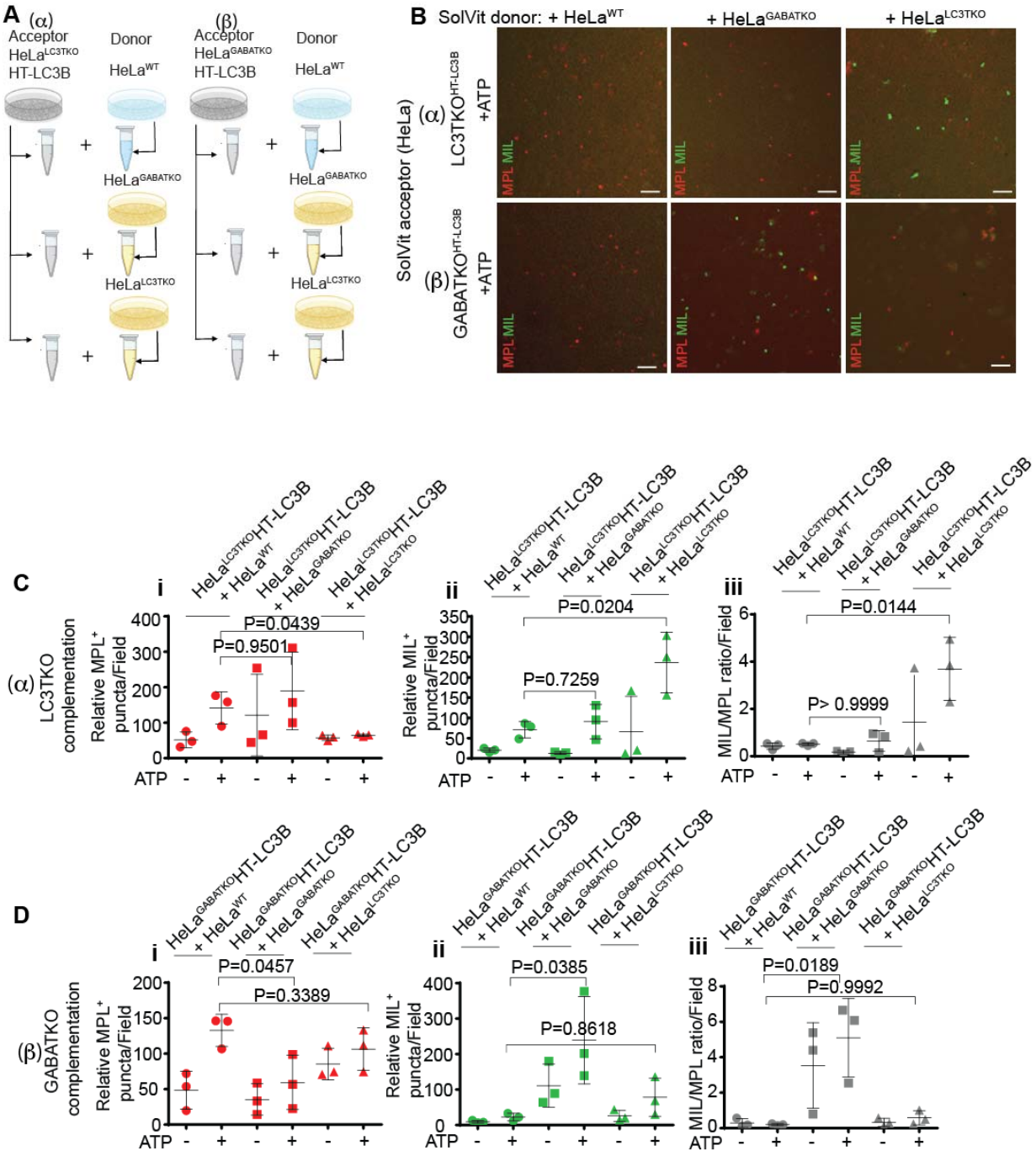

Figure 4. GABARAP and LC3 subsets contribute to membrane imperviousness.

(A) Schematics of in vitro complementation/rescue in the SolVit system: (C-α) HeLa^{LC3TKO}-HT-LC3B PNS (acceptor) with HeLa^{WT}, Hela^{GABATKO} or HeLa^{LC3TKO} PNS (donors); (C-β) HeLa^{GABATKO}-HT-LC3B PNS (acceptor) with HeLa^{WT}, Hela^{GABATKO} or HeLa^{LC3TKO} PNS (donors).

(B) HCM images, examples from SolVit experiments. Red puncta, MPL^+ (LC3B sealed membranes); green puncta, MIL^+ (LC3B unsealed membranes), Scale bars: 3 μm
(C) SolVit complementation/rescue analysis (quantification) of acceptor $HeLa^{LC3TKO}$-HT-LC3B PNS with donor PNS from $HeLa^{WT}$, $HeLa^{LC3TKO}$ or $Hela^{GABATKO}$ cells ±ATP, 1 h, 37˚C.
(D) SolVit complementation/rescue analysis (quantification) of acceptor $HeLa^{GABATKO}$-HT-LC3B PNS with donor PNS from $HeLa^{WT}$, $HeLa^{LC3TKO}$ and $Hela^{GABATKO}$ cells ±ATP, 1 h, 37˚C.
Statistical significance was determined by one-way ANOVA followed by Tukey's multiple comparison test. All values are mean ± SD, n = 3 biologically independent replicates, each HCM experiment: 1,000 valid primary objects/well, 5 wells/sample.

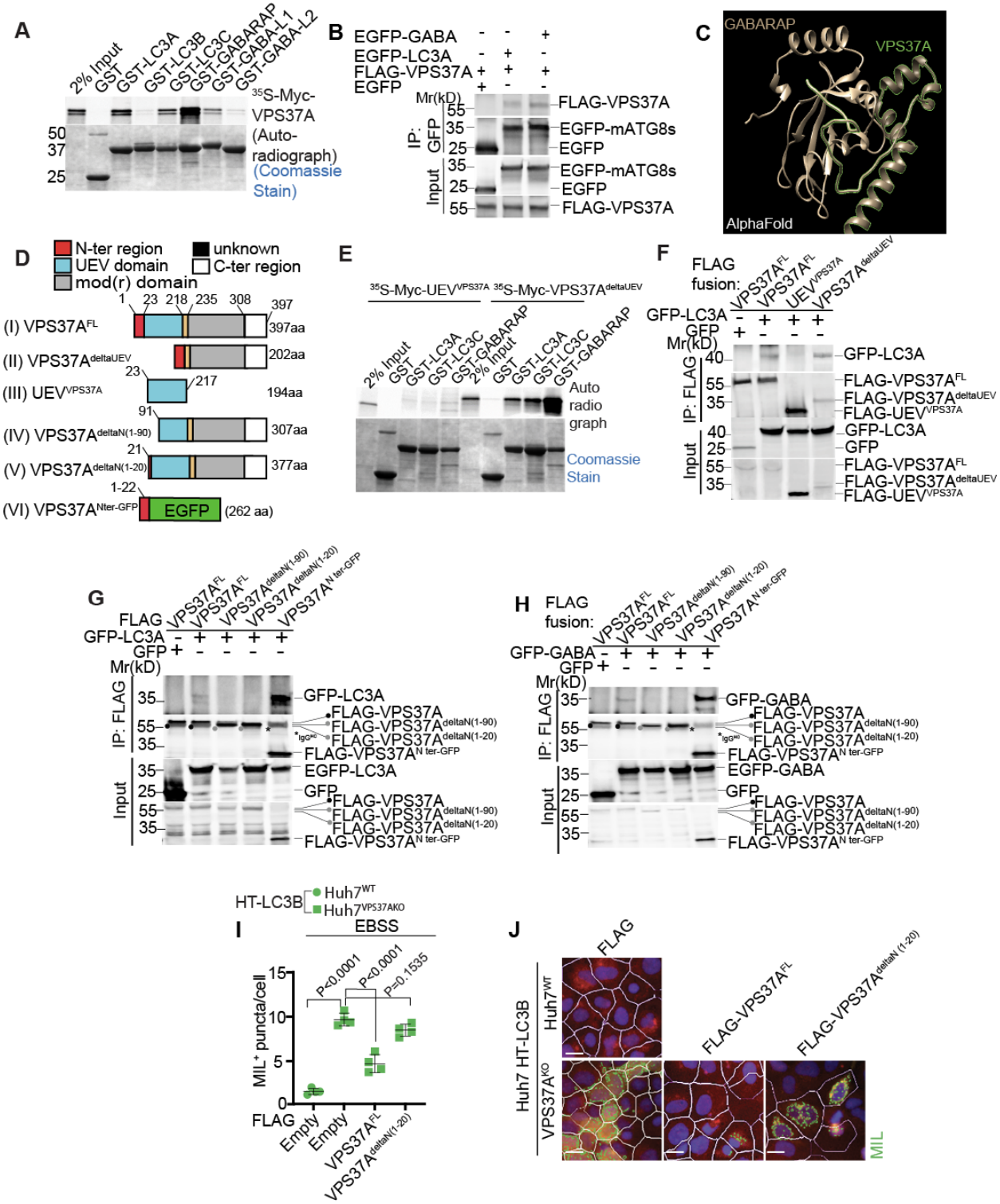

Figure 5. mATG8s interact with ESCRT I component VPS37A

(A) GST pulldown analysis of *in vitro* translated and radiolabeled [^{35}S] Myc–VPS37A with GST or GST tagged LC3A, LC3B, LC3C, GABARAP, GABARAP-L1 and GABARAP-L2**.** 2% of input was loaded.

(B) Co-IP analysis of interactions between FLAG-VPS37A, GFP-LC3A and GFP-GABARAP(GABA) in HEK293T cells. 5% of input was loaded.
(C) AlphaFold predicted complexes between VPS37A^{deltaUEV} and GABARAP.
(D) Schematic of VPS37A full length and deletion constructs: (I) VPS37A^{FL} (full length), (II) VPS37A^{deltaUEV} deletion of UEV (cyan), (III) UEV^{VPS37A}, UEV domain (cyan) only, (IV) VPS37A$^{deltaN(1-90)}$ deletion of residues 1-90, (V) VPS37A$^{deltaN(1-20)}$, deletion of residues 1-20 (red), (VI) VPS37A$^{Nter-EGFP}$, N-ter 1-22 chimera with GFP.
(E) GST-Pull down of Myc-UEV^{VPS37A} and Myc-VPS37A^{deltaUEV} with GST or GST-LC3A, GST-LC3C and GST-GABARAP, 2% of input was loaded.
(F) Co-IP between GFP-LC3A with FLAG-VPS37A^{FL}, UEV^{VPS37A} and VPS37A^{deltaUEV}.
(G) Co-IP analyses in HEK293T cells expressing FLAG-VPS37A^{FL}, FLAG-VPS37A$^{deltaN(1-90)}$, VPS37A$^{deltaN(1-20)}$ and FLAG-Nter-EGFP and co-transfected with GFP-GABA. 5% of input was loaded.
(H) Co-IP analyses in HEK293T cells expressing FLAG-VPS37A^{FL}, FLAG-VPS37A$^{deltaN(1-90)}$, VPS37A$^{deltaN(1-20)}$ and FLAG-Nter-EGFP and co-transfected with GFP-LC3A. 5% of input was loaded.
(I) Complementation of VPS37A KO with VPS37A constructs that have or lack mATG8-binding region. Quantification of MIL^{+} puncta in Huh7^{WT} HT-LC3B (circles) and Huh7^{VPS37AKO} HT-LC3B cells (squares), transfected with empty FLAG, full length VPS37A (FLAG-VPS37A^{FL}) or mutant VPS37A (FLAG-VPS37A$^{deltaN(1-20)}$). Statistical significance was determined by one-way ANOVA followed by Tukey's multiple comparison test. All values are means ± SD, n = 3 biologically independent replicates, each HCM experiment: 1,000 valid primary objects/well, 6 wells/sample.
(J) HCM images, examples corresponding to Fig 5I, scale bar: 10 μm.

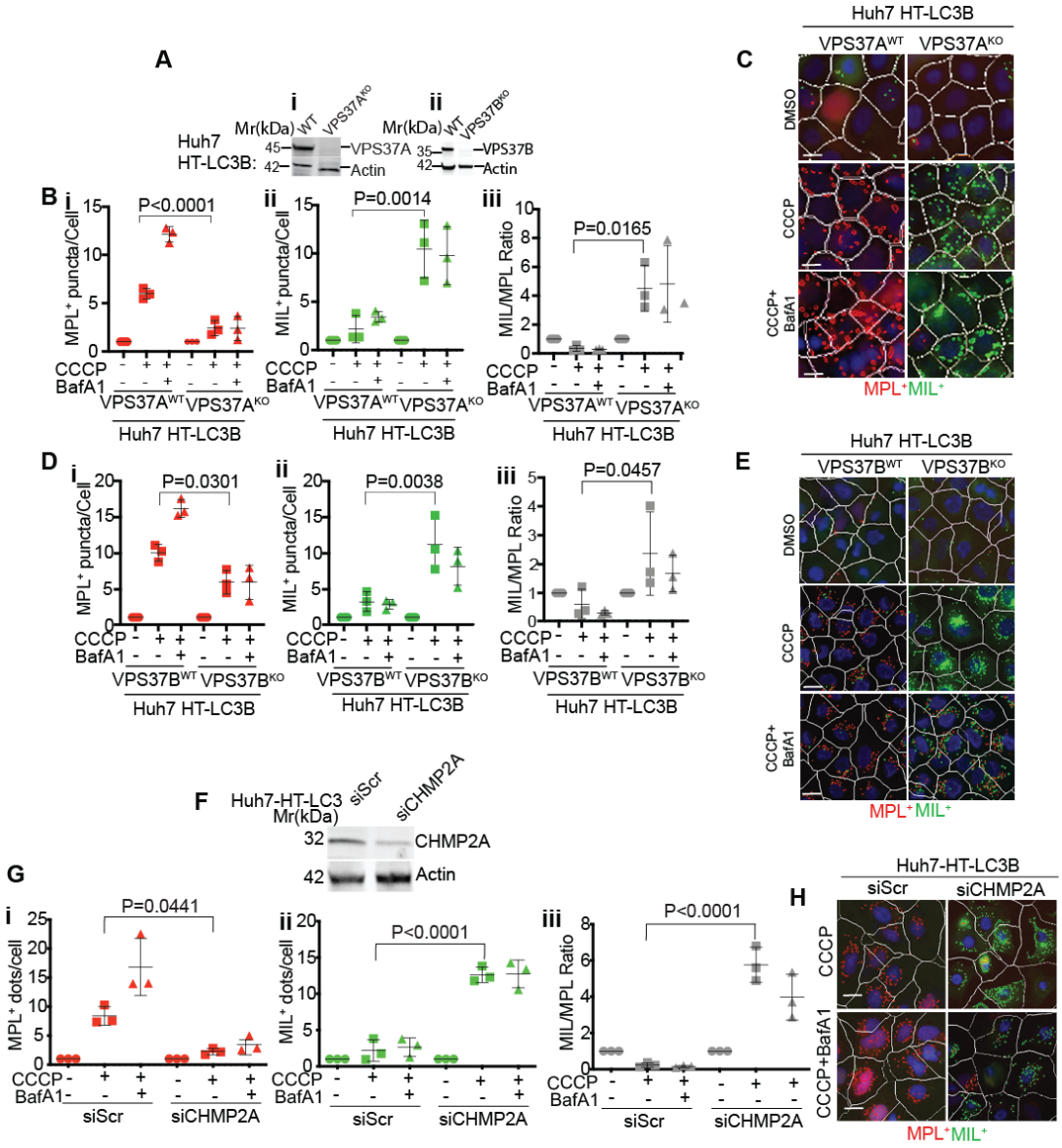

Figure 6. ESCRT components contribute to autophagosomal membrane imperviousness during mitophagy

(A) Western blot of Huh7^{WT} and Huh7^{VPS37AKO} (A i) and Huh7^{VPS37BKO} (A ii) stably expressing HT-LC3B.
(B) MPL-MIL HCM assay in Huh7^{WT} and Huh7^{VPS37AKO} stably expressing HT-LC3B. Quantification: (B i) membrane-permeant HT ligand (MPL) staining of LC3B-II sequestered within sealed membranes. (B ii) MIL staining of membrane-bound HT-LC3B-II accessible to the cytosol and (B iii) MIL/MPL puncta ratio.
(C) HCM images representing MPL^{+} (sealed) or MIL^{+} (unsealed or otherwise accessible LC3B) membranes after induction of mitophagy by CCCP (20 µM) in ±100 nM BafA1. Huh7^{WT} and Huh7^{VPS37AKO} cells stably expressing HT-LC3B.

(D) MPL-MIL HCM assay in Huh7^{WT} and Huh7^{VPS37BKO} stably expressing HT-LC3B during CCCP-induced mitophagy in ± BafA1 (100 nM). Quantification: (D i) MPL^{+} sealed membranes in Huh7^{WT} and Huh7^{VPS37BKO} HT-LC3B (D ii) MIL^{+} unsealed membranes and, (D iii) MIL/MPL puncta ratio**.**
(E) HCM images representing MPL^{+} sealed membrane and MIL^{+} unsealed membrane after induction of mitophagy by CCCP (20 μM) in ± BafA1 (100 nM) in Huh7^{WT} and Huh7^{VPS37BKO} stably expressing HT-LC3B cells.
(F-H) MPL-MIL HCM assay in Huh7^{WT} (control or CHMP2A siRNA-treated cells; immunoblot in F) stably expressing HT-LC3B during CCCP-induced mitophagy in ± BafA1 (100 nM). (G) Quantification: (G i) MPL^{+} sealed membranes; (G ii) MIL^{+} unsealed membranes; (G iii) MIL/MPL puncta ratio**.** (H) HCM images corresponding to panel G.
Statistical significance was determined by one-way ANOVA followed by Tukey's multiple comparison test. All values are mean ± SD, n = 3 biologically independent experiments, each HCM experiment: 1,000 valid primary objects/cells per well, 6 wells/sample**.**

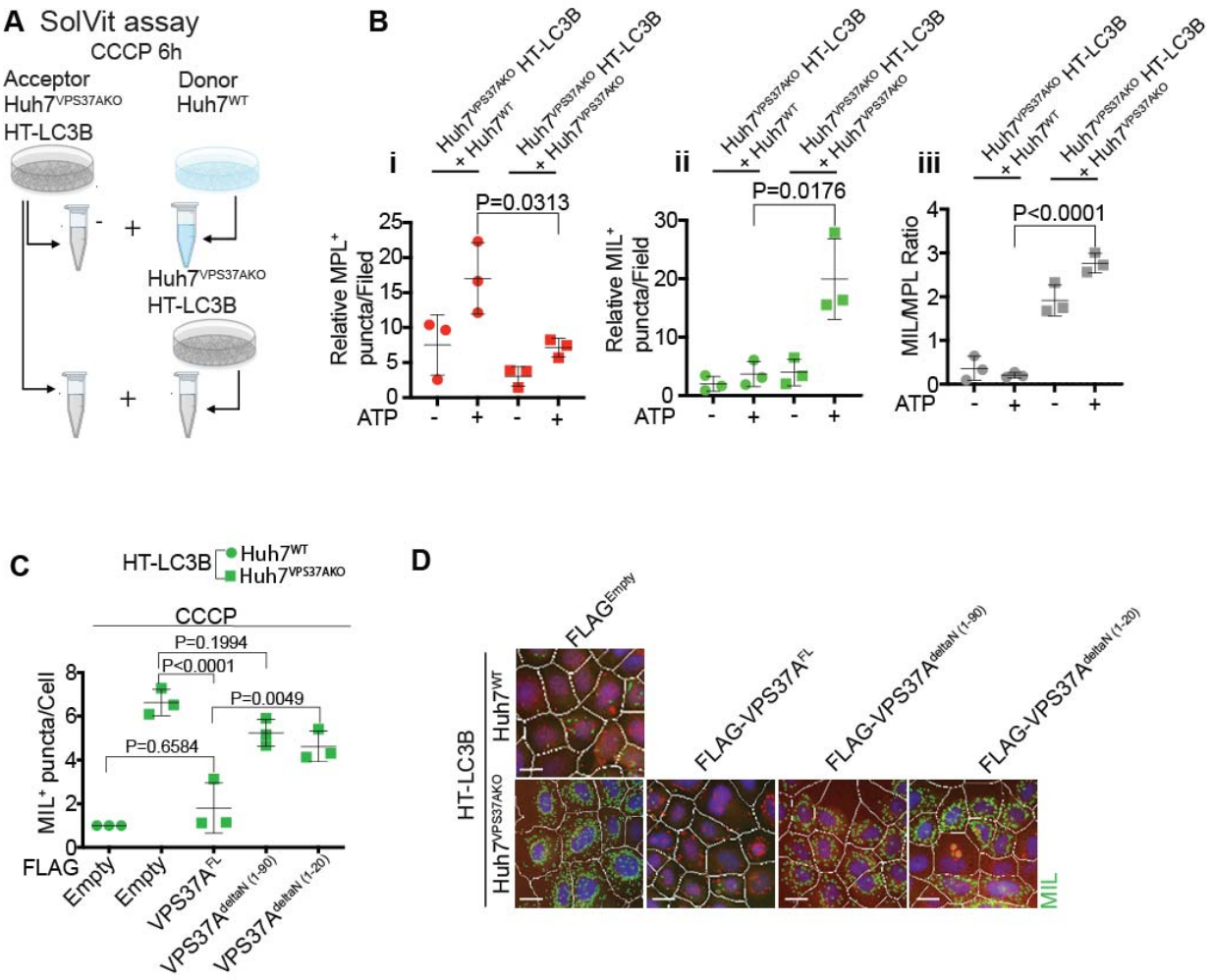

Figure 7. VPS37A restores membrane integrity in vitro and its ATG8-interaction domain is critical to maintain impermeability of autophagic membranes in cells.

(A) Schematic representation, SolVit system for Huh7^{VPS37AKO} HT-LC3B. Huh7^{VPS37AKO} HT-LC3B cells were treated with CCCP (20μM) for 6h and post nuclear supernatant (PNS) was collected by centrifugation at 12,000g. PNS of Huh7^{VPS37AKO} HT-LC3B stable expressing HT-LC3B was incubated *in vitro* with Huh7^{WT} and Huh7^{VPS37AKO} PNS in presence and absence of ATP for 1h. PNS mix products were stained with MIL to label membrane-bound HT-LC3-II and fixed with 4% PFA, samples were then treated with MPL to stain LC3-II that is sequestered within the membranes.
(B) Quantification of puncta: (B-i) MPL^{+} puncta (red), sealed LCB^{+} membranes; (B-ii) MIL^{+} (green) puncta, unsealed/ligand-accessible LCB^{+} membranes; (B-iii) MIL/MPL ratios (gray).
(C) Quantification of MIL^{+} puncta (unsealed/ligand-accessible LC3B^{+} membranes) in Huh7^{WT} (circles) or Huh7^{VPS37AKO} (squares) cells stably expressing HT-LC3B. Cells were transfected with empty FLAG vector, FLAG-VPS37A full length (VPS37A^{FL}), FLAG-VPS37A$^{deltaN(1-90)}$, or FLAG-VPS37A$^{deltaN(1-20)}$ constructs. CCCP, 6 h treatment.

(D) HCM images of Huh7^{VPS37AKO} HT-LC3B with VPS37A constructs (VPS37A^{Full}, FLAG-VPS37A$^{deltaN(1-90)}$, FLAG-VPS37A$^{deltaN(1-20)}$ and FLAG-VPS37A$^{Nter-GFP}$). FLAG-Tag VPS37A constructs, expression detected as red; and MIL^{+} puncta, pseudo color green. Statistical significance was determined by one-way ANOVA followed by Tukey's multiple comparison test. All values are mean ± SD, n = 3 biologically independent experiments, each HCM experiment: 1,000 valid primary objects/cells per well, 6 wells/sample, Scale bars, 10μm.

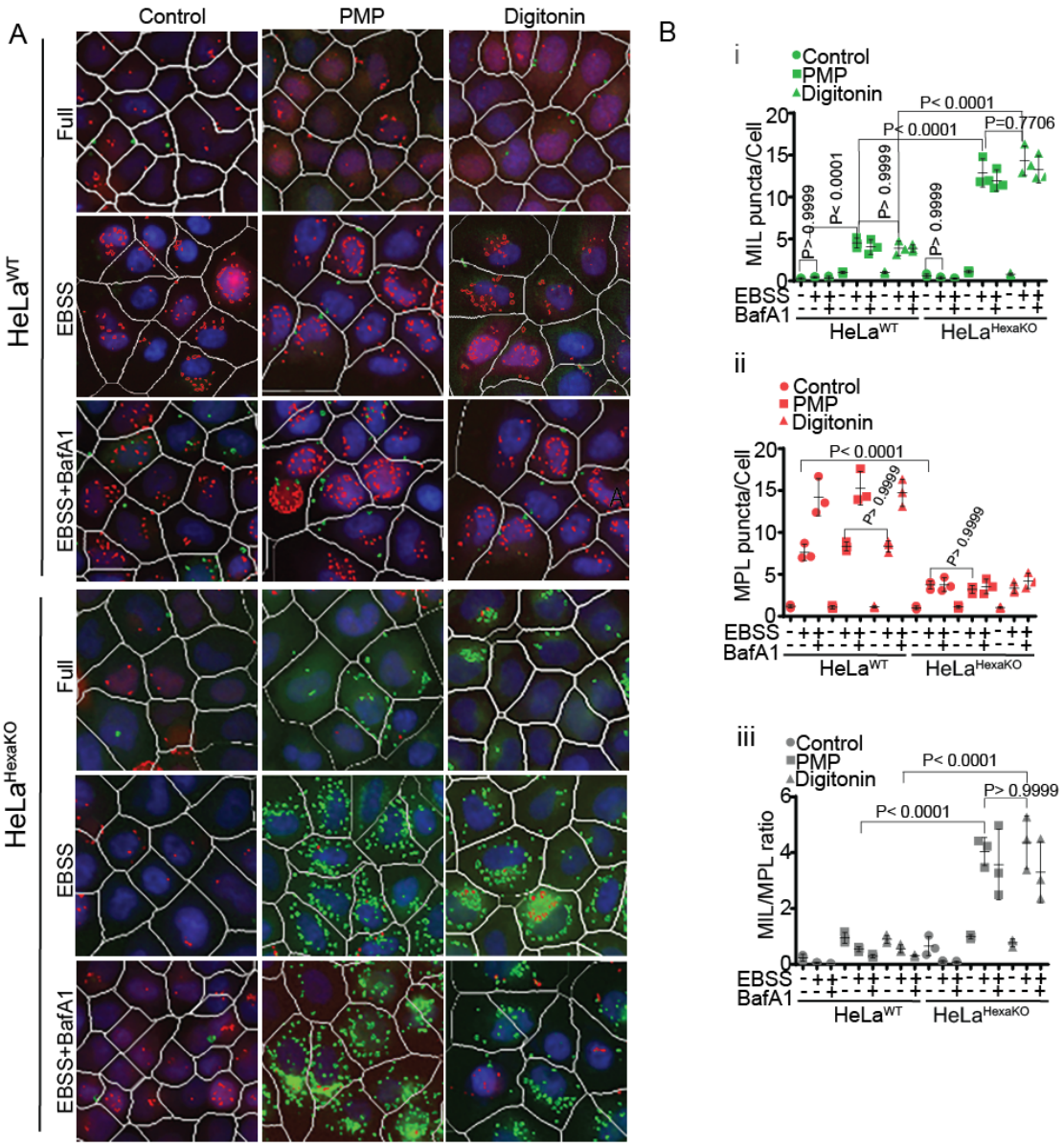

Figure EV1. Analysis of the specifity of MIL/MPL assay

(A) HeLa^{WT} or HeLa^{HexaKO} cells were starved in EBSS for 90 min ±100 nM BafA1, permeabilized or nonpermeabilized (control) as indicated and sequentially incubated with MIL and MPL. For permeabilization, 4 nM PMP (XF Plasma Membrane Permeabilizer (PMP) or 2 µM digitonin were used.
(B) HCM images (masks: white, primary objects/cells; red, MPL profiles; green, MIL profiles), MIL and MPL profiles quantified by HCM, MIL (B i; green), marker of sealed membranes; MPL (B ii; red), marker of unsealed membranes; (B iii) MIL+/MPL+ puncta ratio (gray). Images, one of 80 fields/well, 1,000 primary objects (cells) per well; 6 wells per plate (sampling error), triplicate plates (independent biological replicates). Statistical

significance was determined by one-way ANOVA followed by Tukey's multiple comparison test. All values are mean ± SD, n = 3 biologically independent experiments.

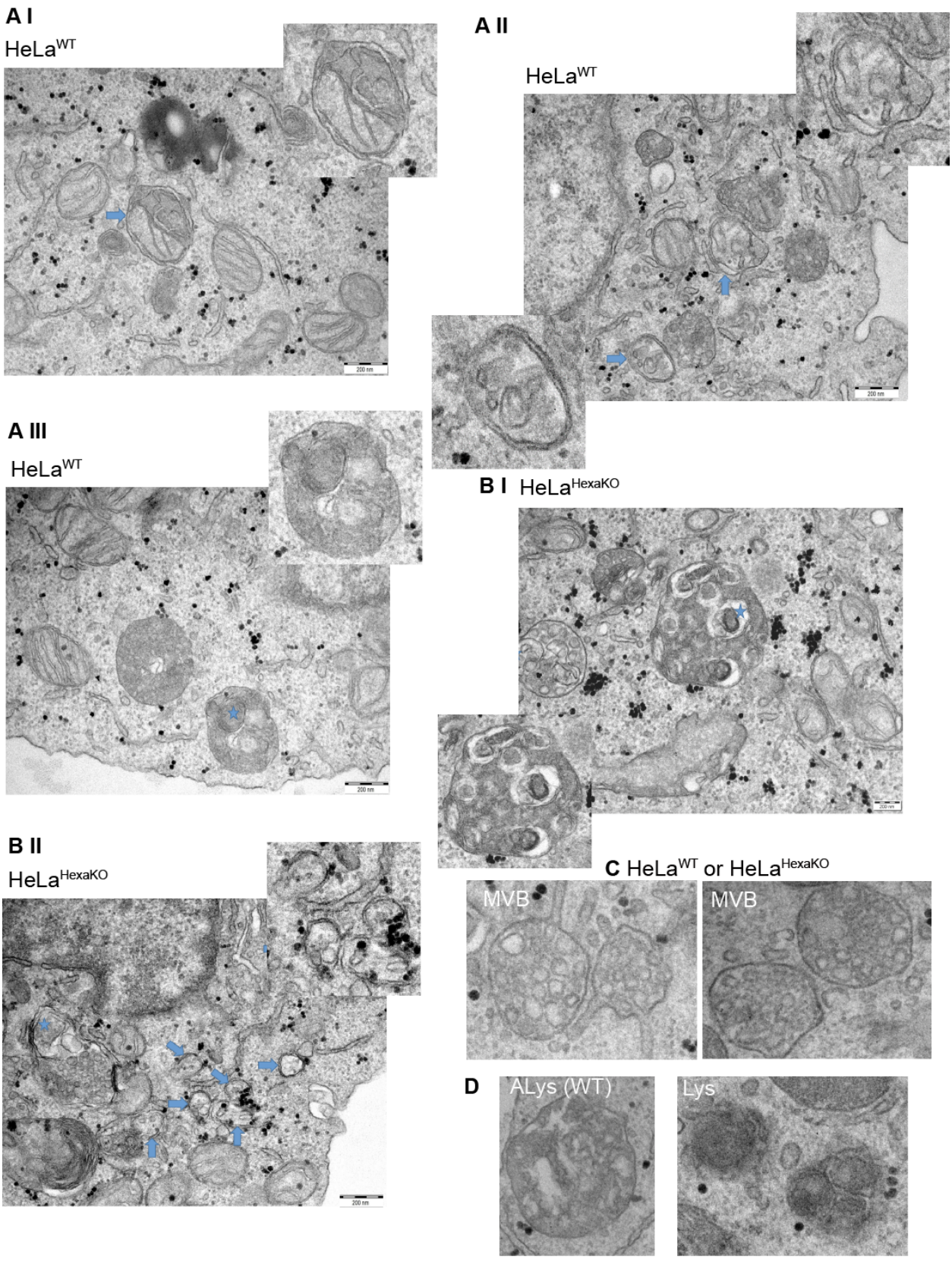
A I
HeLa^WT
A II
HeLa^WT
A III
HeLa^WT
B I HeLa^HexaKO
B II
HeLa^HexaKO
C HeLa^WT or HeLa^HexaKO
MVB
MVB
D
ALys (WT)
Lys

Figure EV2. Ultrastructural analysis of organelles in HeLa^{WT} and HeLa^{HexaKO} cells.

(A and B) Electron microscopy (EM) images of autophagic organelles in cells induced for autophagy by starvation in EBSS for 90 min (see Fig 1). Blue arrows: autophagosomal structures (autophagosomes and phagophores). Blue asterisks: amphisomes.
(A) HeLa^{WT} (A I-III);
(B) HeLa^{HexaKO} (B I,II)
(C) MVB/endosomes (no differences noted between HeLa^{WT} and HeLa^{HexaKO} cells)
(D) Lysosomal structures: ALys, autolysosomes (HeLa^{WT}). Lys, lysosomes. Electron-dense dots, glycogen granules. Scale bar: 200 nm.

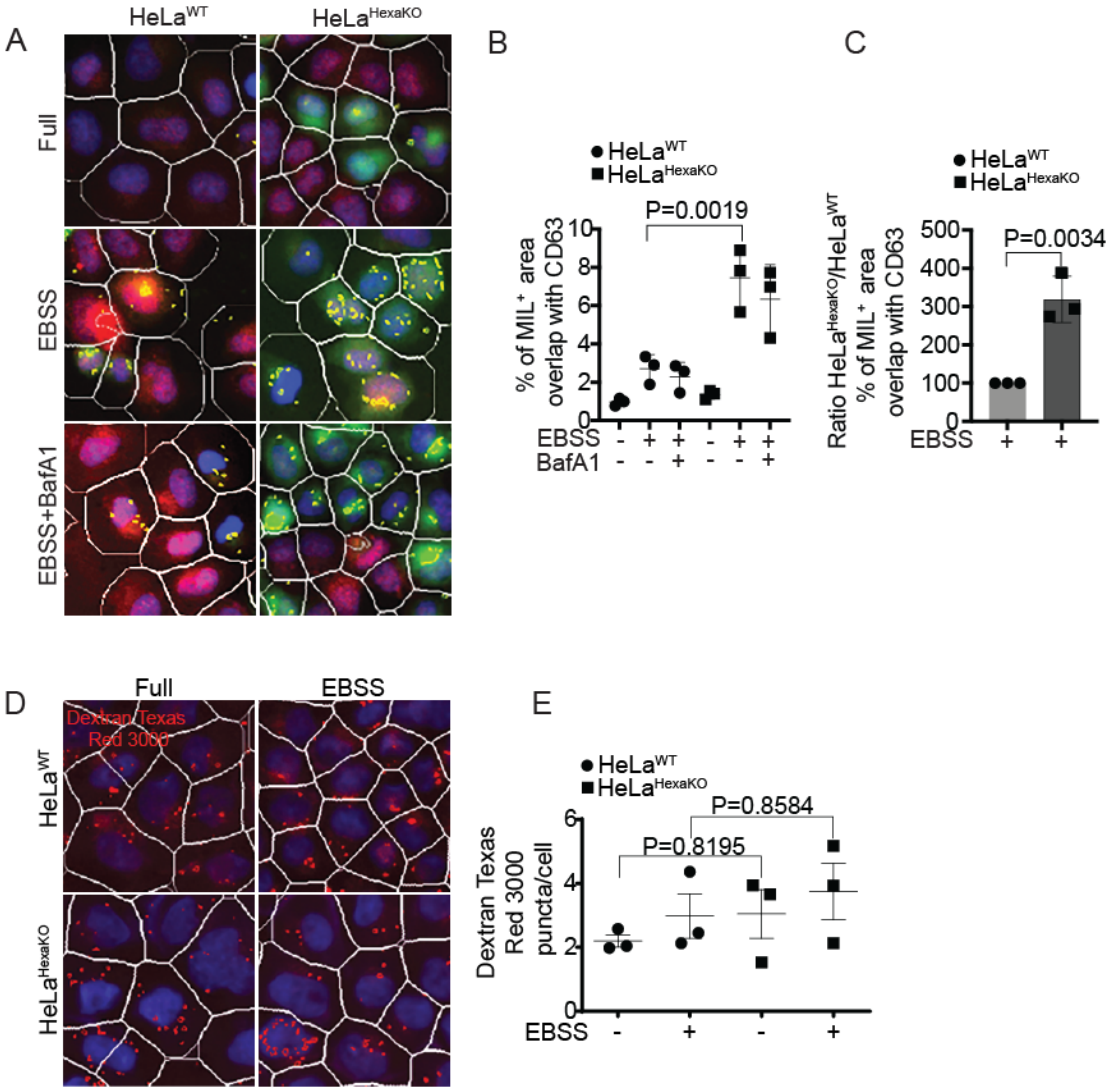

Figure EV3. Analysis of MIL $^{+}$ colocalization with CD63 and endocytic uptake in cells lacking mAtg8s.

(A) HeLa^{WT} or HeLa^{HexaKO} cells were starved in EBSS for 90 min ±100 nM BafA1, permeabilized and exposed to MIL for 15 min at 37˚C. Cells were blocked in 3% BSA with 0.05% saponin for 30 min followed by incubation with primary antibody for overnight at 4˚C and secondary antibody for 1 h at RT. HCM images (masks: white, primary objects/cells; red, CD63 profiles; green, MIL profiles), One of 80 fields/well,
(B) MIL and CD63 overlap (Yellow masks) quantified by HCM. 1,000 primary objects (cells) per well; 6 wells per plate (sampling error), triplicate plates (independent biological replicates). Statistical significance was determined by one-way ANOVA followed by Tukey's multiple comparison test. All values are mean ± SD, n = 3 biologically independent experiments.
(C) Normalized replot of data in panel B. t-test.

(D) HeLa^{WT} or HeLa^{HexaKO} cells were starved in EBSS for 60 min; cells were allowed to endocytose Dextran, Texas Red™, 3000 MW in PBS for 30 min at 37˚C. Cells were fixed with 4% PFA for 5 min. HCM images (masks: white, primary objects/cells; red, Dextran, Texas Red™ puncta).
(E) Dextran puncta were quantified by HCM. 1,000 primary objects (cells) per well; 6 wells per plate (sampling error), triplicate plates (independent biological replicates). Statistical significance was determined by one-way ANOVA followed by Tukey's multiple comparison test. All values are mean ± SD, n = 3 biologically independent experiments.

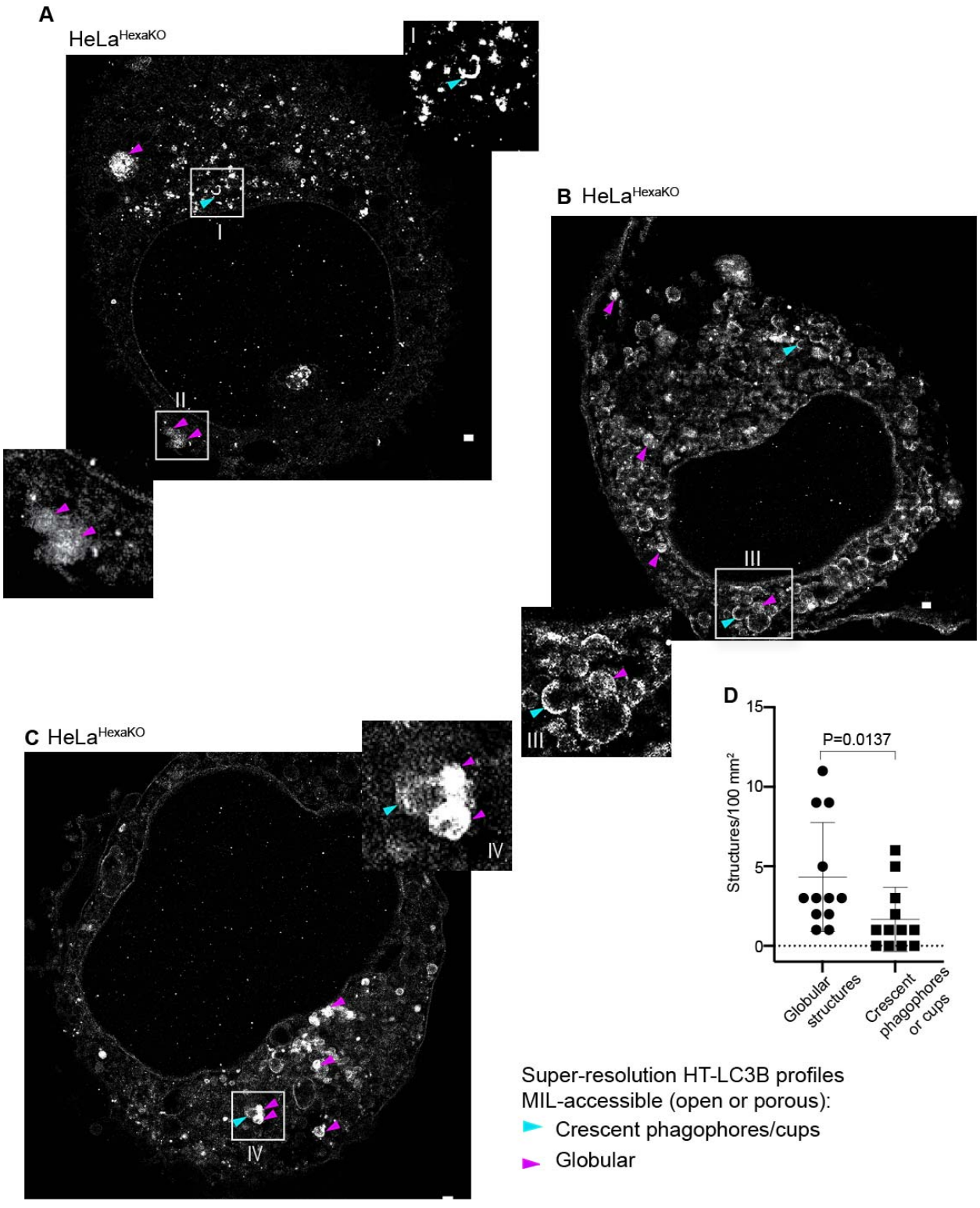

Figure EV4. Super-resolution microscopy (dSTORM) reveals a spectrum of permeant membranous structures in cells devoid of principal mATG8s.

(A to C) HeLa^{HexaKO} cells stably expressing HT-LC3B were starved in EBSS for 90 min to induce autophagy. After selective permeabilization of plasma membrane, cells were then stained with membrane-impermeable HT ligand (MIL; Alexa fluor 660) and processed for super-resolution microscopy (dSTORM; see methods). White rectangles; zoomed insets. Cyan arrowheads; crescent structures (phagophores). Magenta arrowheads; globular structures with internal membranes accessible to the MIL probe.
(D) Quantification of globular and crescent/cup structures. 12 randomly positioned squares of 100 μm^2 (n=3; SR images). Data points represent each of the 12 squares, containing Y-axis of profiles with type specified on the X axis. Statistical significance was determined by t test followed by nonparametric Mann-Whitney t-test comparison test. All values are mean ± SD, Scale bar: 1 μm.
Note: The inset in B emphasizes the appearance of crescents whereas the graph in D represents the quantitative measures and statistical analysis.

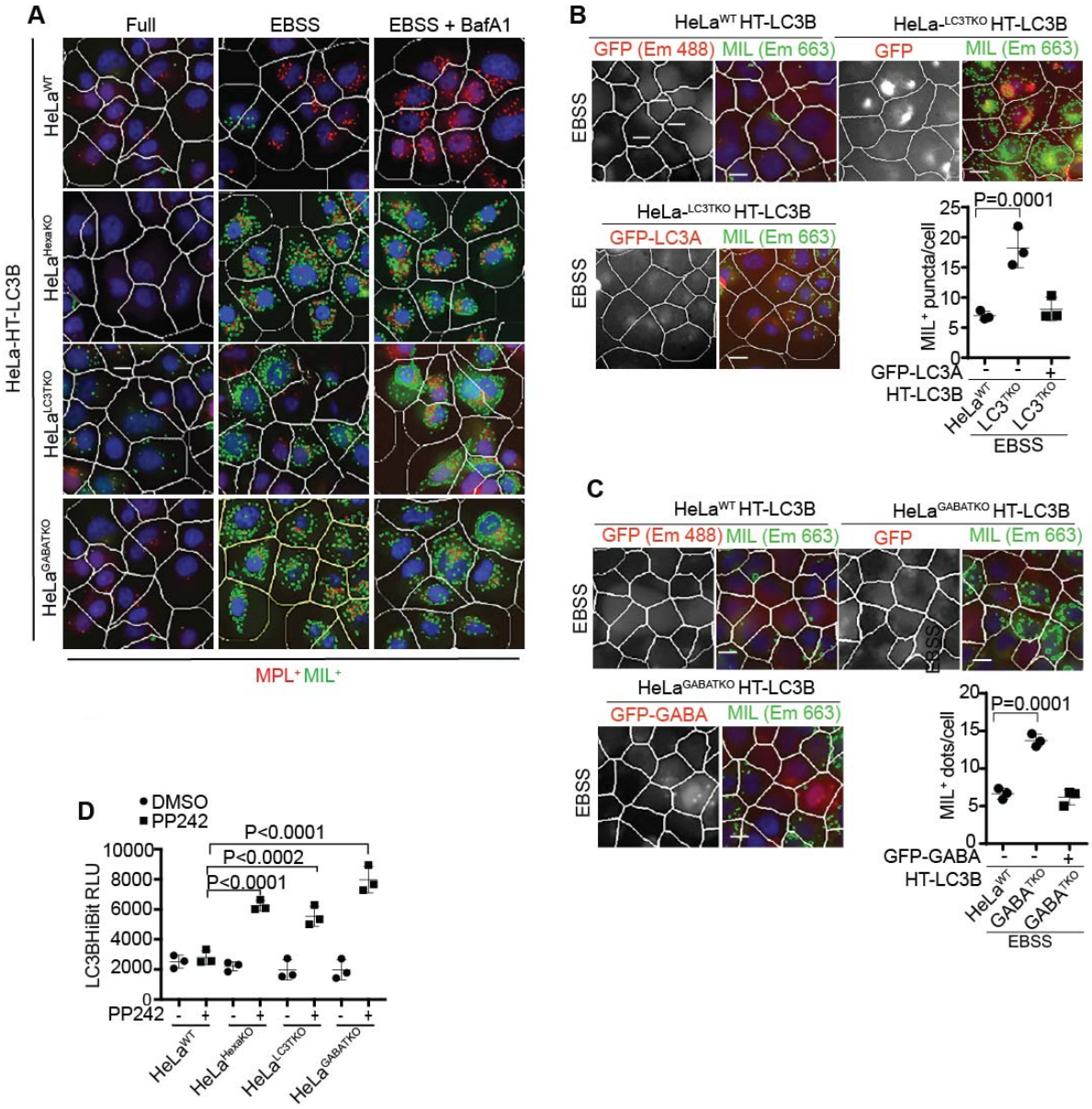

Figure EV5. Both GABARAP and LC3 subsets of mATG8s maintain the integrity of LC3B$^+$ membranes.

(A) HeLa^{WT}, HeLa^{HexaKO}, HeLa^{LC3TKO} and HeLa^{GABATKO} stably expressing HT-LC3B were starved to induced autophagy in EBSS 90 min ±100 nM BafA1. MPL-MIL HCM: HCM images representing MPL$^+$ (red) LC3B$^+$ sealed membrane (LC3B sequestered within the sealed membranes). MIL$^+$ (green) LC3B$^+$ unsealed membrane. Scale bars: 10 μm
(B) HeLa^{LC3TKO} expressing HT-LC3B cells complemented with LC3A. Cells were transfected with GFP or GFP-LC3A, plasma membrane selectively permeabilized, and

endomembranes stained with MIL. HCM images, GFP or GFP-LC3A transfected cells (red pseudo color). MIL^+ puncta (green pseudo color) were counted and quantified. Graph, MIL^+ puncta/cell in GFP or GFP-LC3A transfected cells (identified by gating).
(C) $HeLa^{GABATKO}$ expressing HT-LC3B complemented with GFP-GABARAP. Cells were transfected with GFP or GFP-GABARAP. HCM images, GFP or GFP-GABARAP transfected cells stained with MIL (red pseudo color). Graph, quantification of MIL^+ puncta/cell (green pseudo color) in GFP or GFP-GABARAP transfected cells. 1,000 primary objects (cells) per well; 6 wells per plate (sampling error), triplicate plates (independent biological replicates). Statistical significance was determined by one-way ANOVA followed by Tukey's multiple comparison test. All values are mean ± SD, n = 3 biologically independent experiments,
(D) $HeLa^{WT}$ and $HeLa^{HexaKO}$ cells were transfected with LC3BHibit plasmid. Cells were induced to autophagy with mTOR inhibitor PP242 (2 μM) for 6 h. Plasma membrane was selectively permeabilized with PMP (4 nM). Bioluminescence was measured in a luminometer plate reader. Circles: control; squares: PP242-treated cells.
Statistical significance was determined by one-way ANOVA followed by Tukey's multiple comparison test. All values are mean ± SD, n = 3 biologically independent experiments, 24 wells/sample. Scale bars: 10 μm

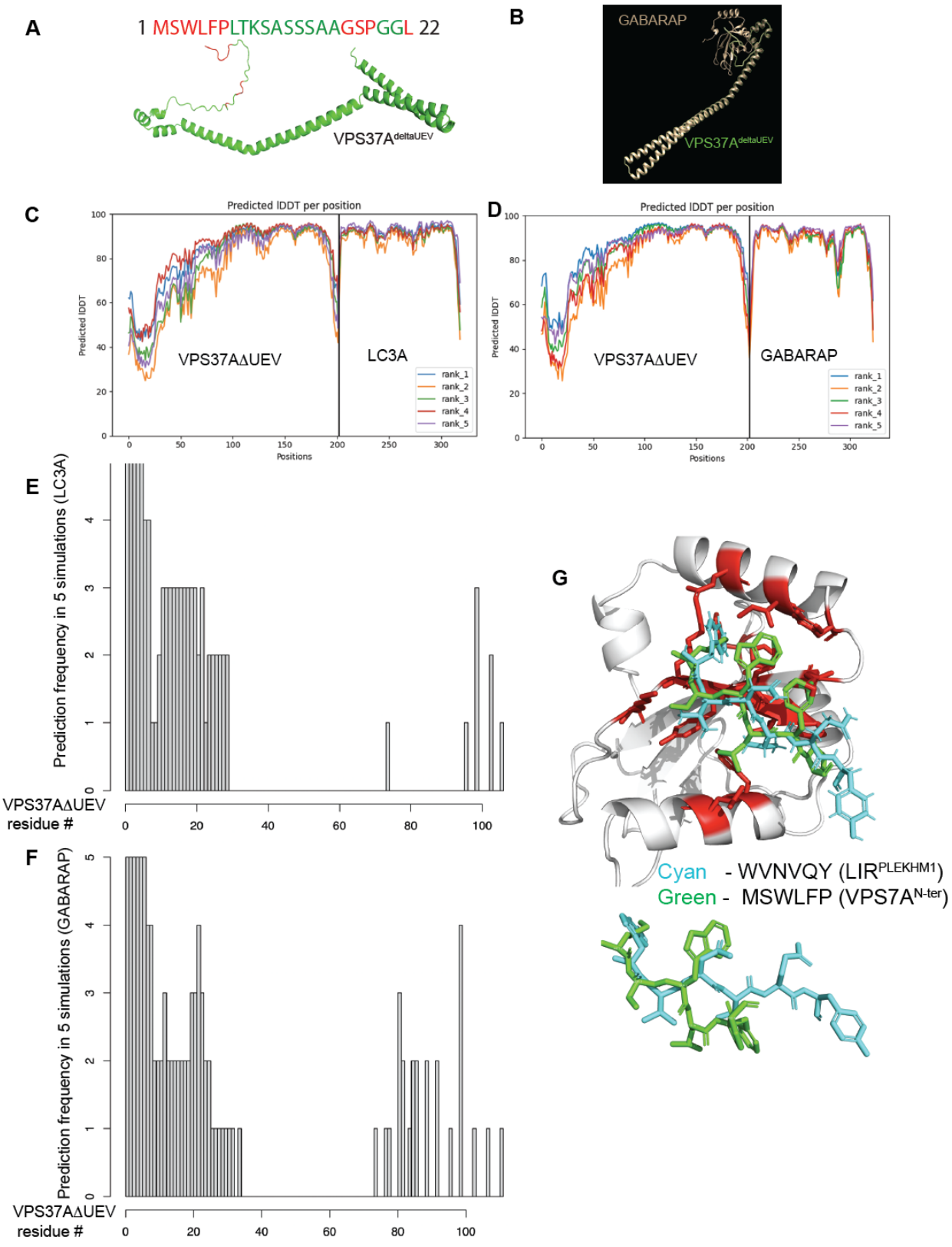

Figure EV6. AlphaFold prediction of VPS37A^{deltaUEV} interactions with mATG8s.

(A) VPS37A^{deltaUEV} AlphaFold-predicted structure; sequence, 1-22 residues, N-terminus of VPS37A (red, residues predicted to contact mATG8s).
(B) Representation of AlphaFold predicted complexes (rank 1; VPS37A^{deltaUEV} and GABARAP).
(C and D) The predicted models re-ranked according to the predicted Local Distance Difference Test score (pLDDT) for each model. ColabFold lDDT graph, all five ranked models and their predicted lDDT C_α score at each residue.
(E and F) Prediction frequencies in 5 simulations of LC3A and GABARAP.
(E) First five long bars of the plot, VPS37A$^{N\text{-}ter}$ residues interacting with LC3A.
(F) First six long bars of the plot, VPS37A$^{N\text{-}ter}$ residues interacting with GABARAP.
(G) Rank 1 model predicted structure showing a sidechain packing within the hydrophobic pocket of GABARAP and LC3A. Cyan, PLEKHM1 LIR peptide (from the known crystal structure of a complex with LC3C). Green, VPS37A$^{N\text{-}ter}$.

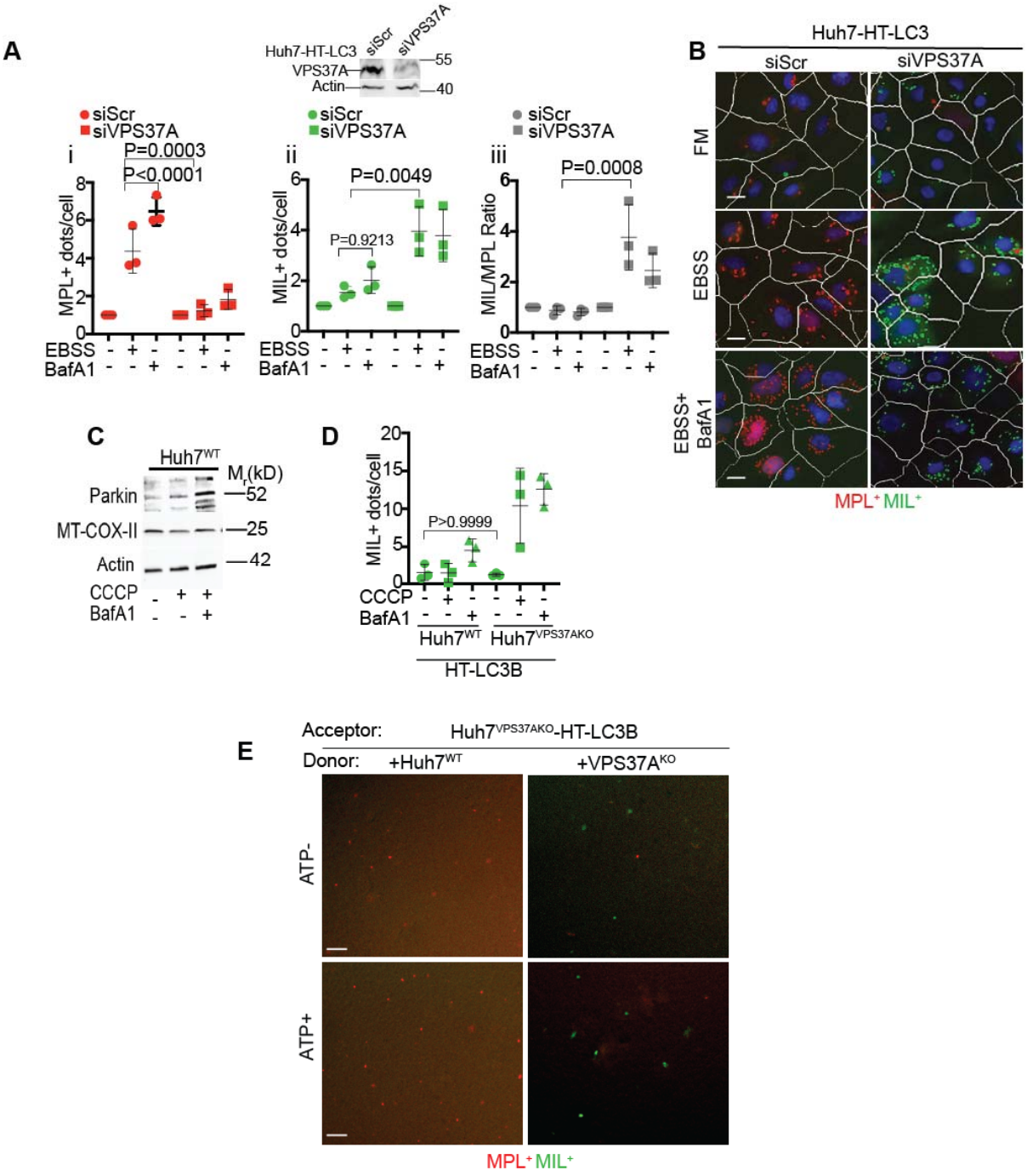

Figure EV7. ESCRT-I protein VPS37A is important to maintain LC3B$^+$ membrane integrity

(A,B) Knockdown of VPS37A in Huh7 HT-LC3B cells and MPL-MIL HCM analysis of membrane permeability. Images and statistics, HCM images (masks: white, primary objects/cells; red, MPL profiles; green, MIL profiles), one of 60 fields/well, 1,000 primary

objects (cells) per well; 6 wells per plate (sampling error), triplicate plates (independent biological replicates).
(C) Western blot analysis of $Huh7^{WT}$ cells under CCCP 6h induced mitophagy conditions in ± BafA1 (100nM); immunoblot indicates accumulation of Parkin and COX-II in the presence of BafA1.
(D) HCM images (one of 60 fields counted) depicting MPL^{+} (sealed) membranes and MIL^{+} (unsealed) $LC3B^{+}$ membranes in ± ATP samples.
(E) Absolute MIL^{+} profile counts corresponding to data in Fig. 6Bii.
Statistical significance was determined by one-way ANOVA followed by Tukey's multiple comparison test. All values are mean ± SD, n = 3 biologically independent experiments.

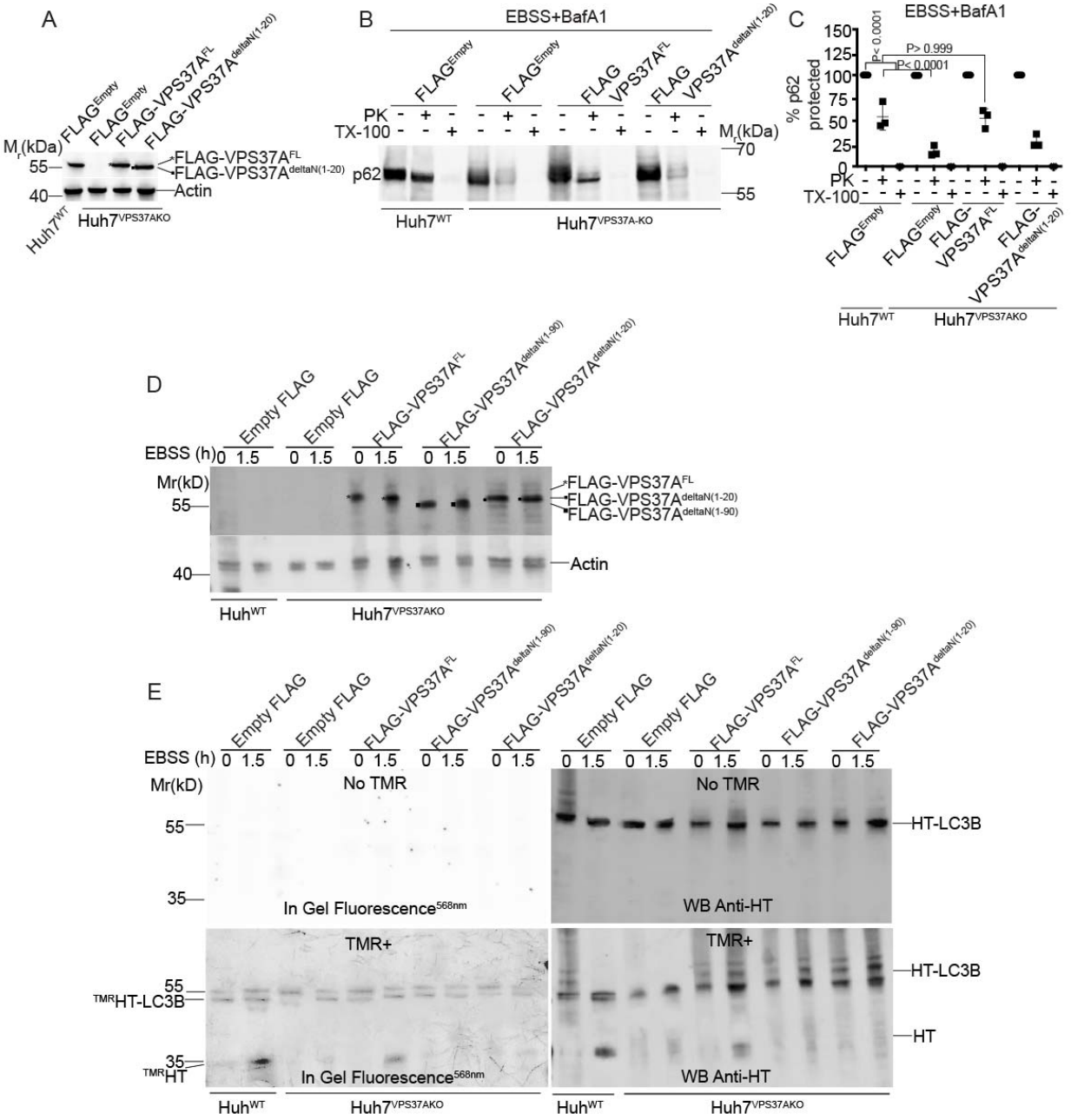

(A) Immunoblot analysis of Huh7^{WT} and Huh7^{VPS37AKO} cells complimented with FLAG-VPS37A^{FL} (Black asterisk), or FLAG-VPS37A$^{deltaN(1-20)}$ (Black circle).
(B) Protease protection assay (Immunoblot analysis of p62 sequestration and protection from proteinase K) in Huh7^{WT} and Huh7^{VPS37AKO}, complimented with FLAG-VPS37A^{FL}, FLAG-VPS37A$^{deltaN(1-20)}$. Cells were starved in EBSS+100nM BafA1 for 90 min. Samples were homogenized and centrifuged at 500 g and supernatant was centrifuged

at 22,000 g for 10 min, pellet was resuspended in homogenization buffer in the presence or absence of 50 mg/ml proteinase K (Pro.K) and 1% Triton X-100 (TX-100) and subjected to the proteinase K protection assay followed by immunoblotting using anti-p62/SQTM1 antibody.
(C) p62 band intensities were quantified and normalized to the respective non-treatment control. Statistical significance was determined by one-way ANOVA followed by Tukey's multiple comparison test. All values are mean ± SD, n = 3 biologically independent experiments.
(D) Immunoblot analysis of Huh7^{WT} and Huh7^{VPS37AKO} cells transfected with Empty-FLAG, FLAG-VPS37A^{FL} (Black asterisk), FLAG-VPS37A$^{deltaN(1-20)}$ (Black circle), or FLAG-VPS37A$^{deltaN(1-90)}$ (Black square). These cells were used in HaloTag^{TMR}-release assay (HTR) in E.
(E) HaloTag^{TMR}-release assay (HTR) assay. Huh^{WT}, Huh7^{VPS37AKO} stably expressing HT-LC3B, transfected with Empty-FLAG, FLAG-VPS37A^{FL}, FLAG-VPS37A$^{deltaN(1-20)}$ or FLAG-VPS37A$^{deltaN(1-90)}$ were starved with EBSS for 90min. Cell were incubated with ± HaloTag ligand fluorescently labeled with TMR for 20-30 min at 37˚C. In-gel fluorescence (TMR) and Western blots (anti-HaloTag antibody) of freed HaloTag^{TMR} were detected.

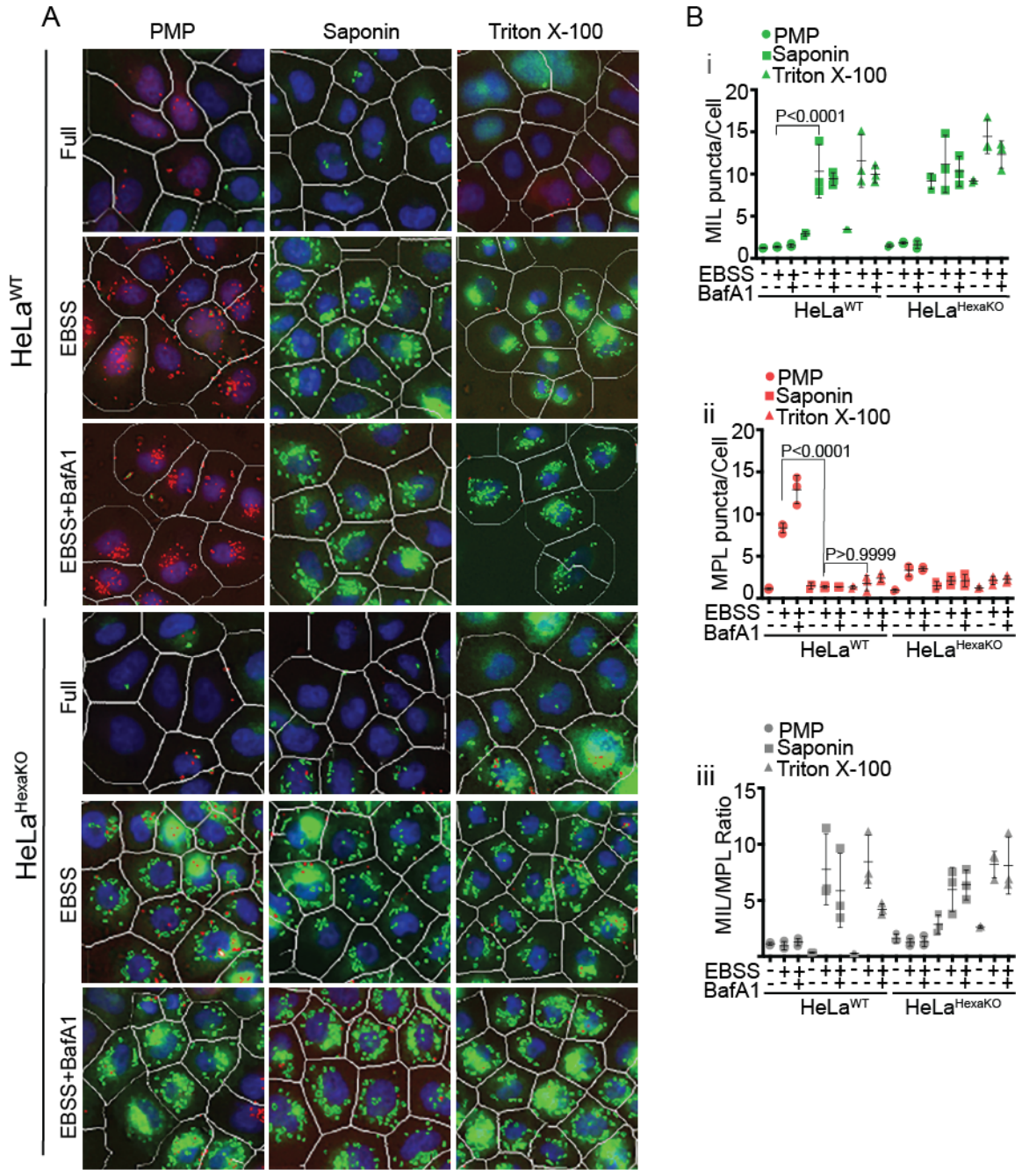

Appendix Figure S1. Comparative selectivity of plasma membrane permeabilizing agent PMP

(A) HeLa^{WT} or HeLa^{HexaKO} cells were starved in EBSS for 90 min ±100 nM BafA1, sequentially incubated with MIL and MPL. Cells were permeabilized with PMP or 0.01% Saponin or 0.1% Triton X-100 for MIL/MPL staining as described in Fig. 1 legend. Examples of HCM images (masks: white, primary objects/cells; red, MPL profiles; green, MIL profiles).

(B) Quantification MIL and MPL profiles by HCM. MIL (B i; green), marker of unsealed membranes; MPL (B ii; red), marker of sealed membranes; (B iii) MIL^{+}/MPL^{+} puncta ratio (gray). HCM images, one of 80 fields/well, 1,000 primary objects (cells) per well; 6 wells per plate (sampling error), triplicate plates (independent biological replicates). Statistical significance was determined by one-way ANOVA followed by Tukey's multiple comparison test (significance cutoff, $P<0.05$). All values are mean ± SD, n = 3 biologically independent experiments.

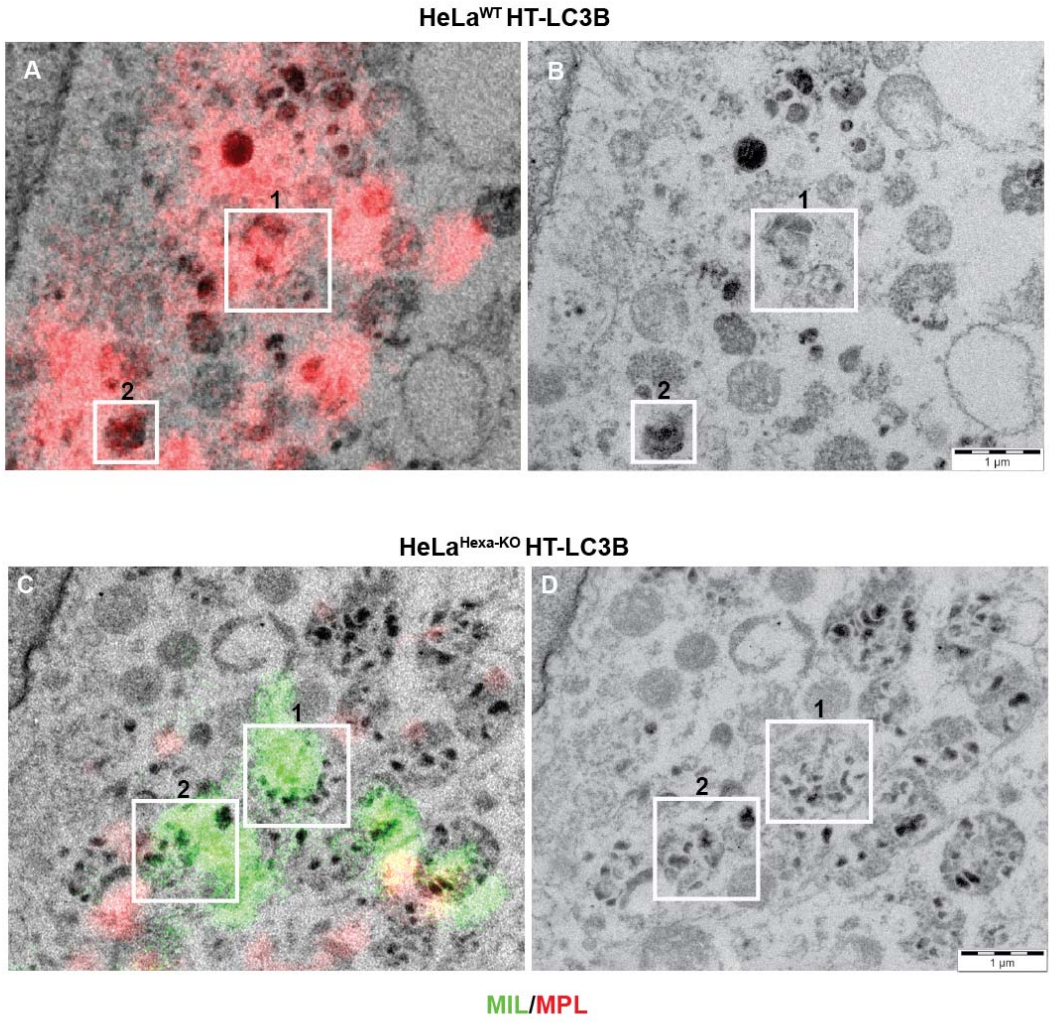

Appendix Figure S2. Correlative light electron microscopy analysis of HaloTag-HT-LC3B organelles.

(A-E) Hela^{WT} cells stably expressing HaloTag-HT-LC3B were starved in EBSS for 90 min and sequentially exposed to HaloTag ligand MIL and MPL. Note that at this incubation time point in WT cells there are nearly exclusive MPL^{+} profiles. Fluorescence image in A is a confocal plane from the z-stack corresponding to EM images in B-E. Numbered boxed areas in A, enlarged sections of the EM micrograph in C-E. Scale bar1 µm.

(F-J) Hela^{HexaKO} cells stably expressing HaloTag-HT-LC3B were starved in EBSS for 90 min and sequentially exposed to HaloTag ligand MIL and MPL. Note that in HeLa^{HexaKO} cells MIL^{+} profiles predominate at this incubation time point. Fluorescence image in F is

a confocal plane from the z-stack corresponding to EM images in G-J. Numbered boxed areas in F, enlarged sections of the EM micrograph in G-J. Scale bar 1µm.

A

HeLa^{HexaKO}

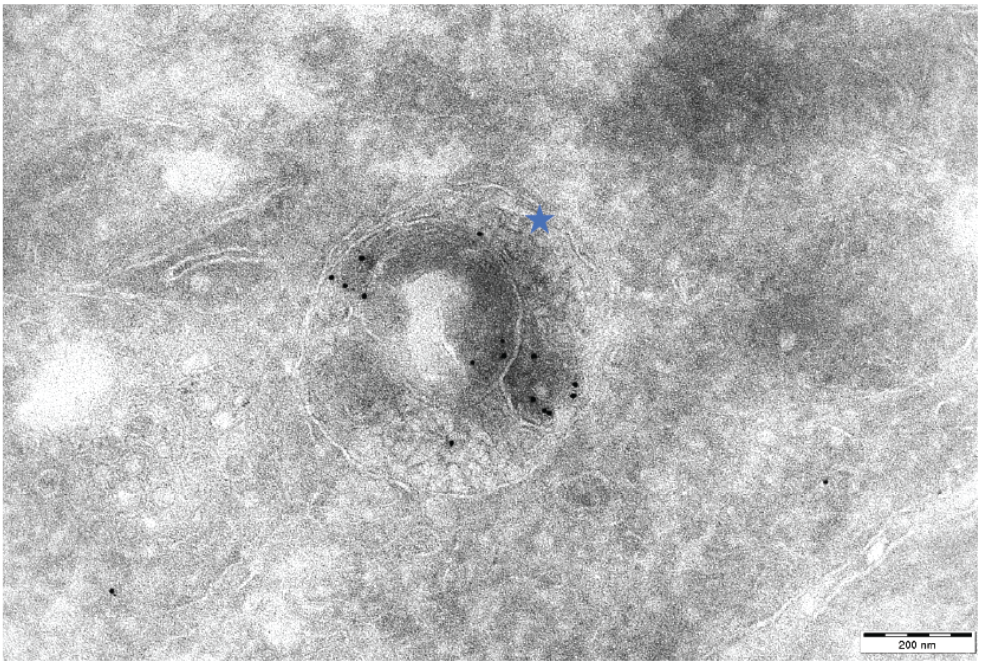

Post-embedding staining gold particles 10nm

B

HeLa^{HexaKO}

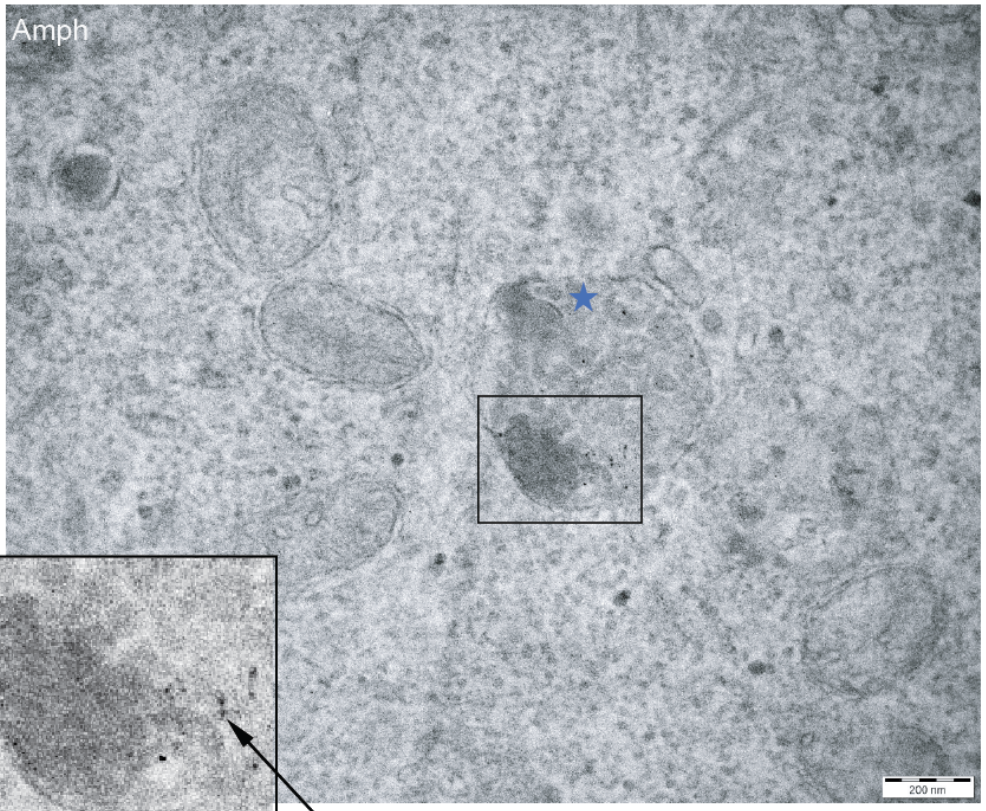

Pre-embedding silver enhanced gold particles 1.2nm

Gold Particle-1.2nm

Appendix Figure S3. Immuno-electron microscopy analysis of autophagic organelles in HeLa^{HexaKO} cells expressing GFP-LC3A.

Autophagy was induced in HeLa^{HexaKO} cells by starvation in EBSS for 90 min.

(A) Post-embedding immuno-EM. The sections were labeled using anti-GFP and 10 nm gold conjugated secondary antibody.

(B) Pre-embedding immuno-EM. (Immunogold, 1.2 nm; gold particles were originally 1.2 nm and silver enhanced to increase visibility). Rectangle, zoomed region. Blue asterisks, amphisomes positive for GFP-LC3A. Scale bars: 200 nm.

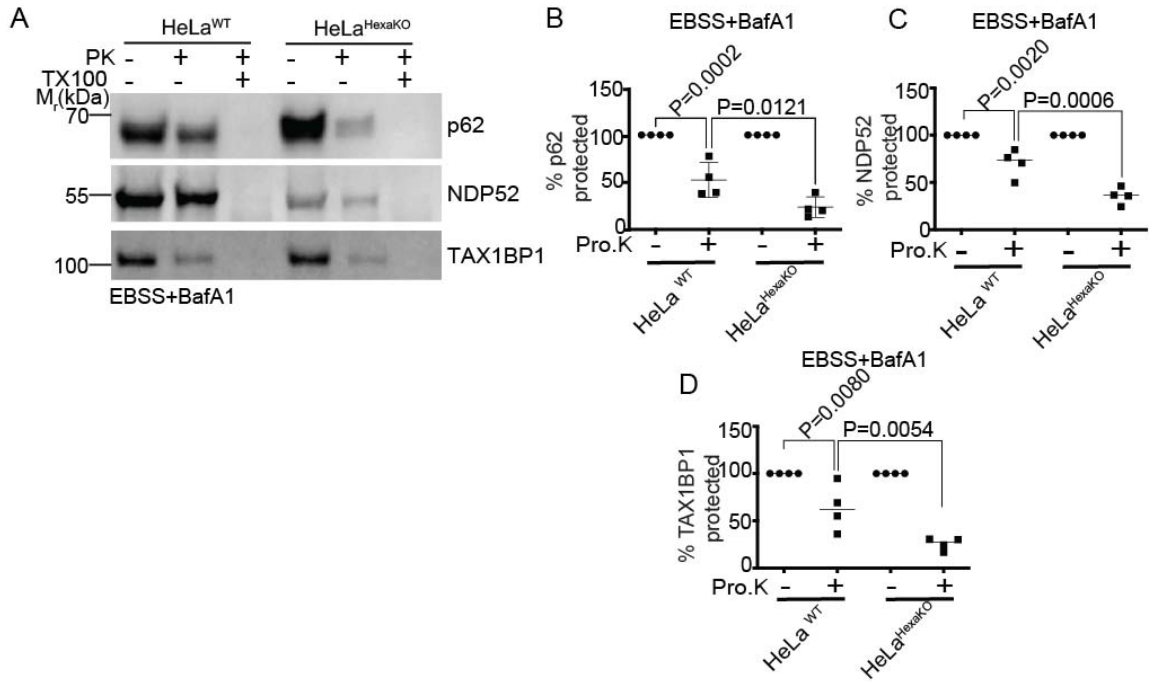

Appendix Figure S4. Proteinase K protection analysis of autophagic receptors p62, NDP52 and TAX1BP1 in HeLa^{WT} and HeLa^{HexaKO} cells.

(A) Protease protection assay in HeLa^{WT} and HeLa^{HexaKO} cells. Cells were starved in EBSS ±100 nM BafA1 for 90 min. Samples were homogenized and centrifuged at 500 g and supernatant was centrifuged at 22,000 g for 10 min, pellet was resuspended in homogenization buffer in the presence or absence of 50 mg/ml proteinase K (Pro.K) and 1% Triton X-100 (TX-100) and subjected to the proteinase K protection assay followed by immunoblotting using anti-p62/SQTM1, NDP52 and TAX1BP1 antibodies.

(B-D) (B) p62 and (C) NDP52 (D) TAX1BP1 levels were quantified and normalized to the respective non-treatment control. Statistical significance was determined by one-way ANOVA followed by Tukey's multiple comparison test. All values are mean ± SD, n = 3 biologically independent experiments.

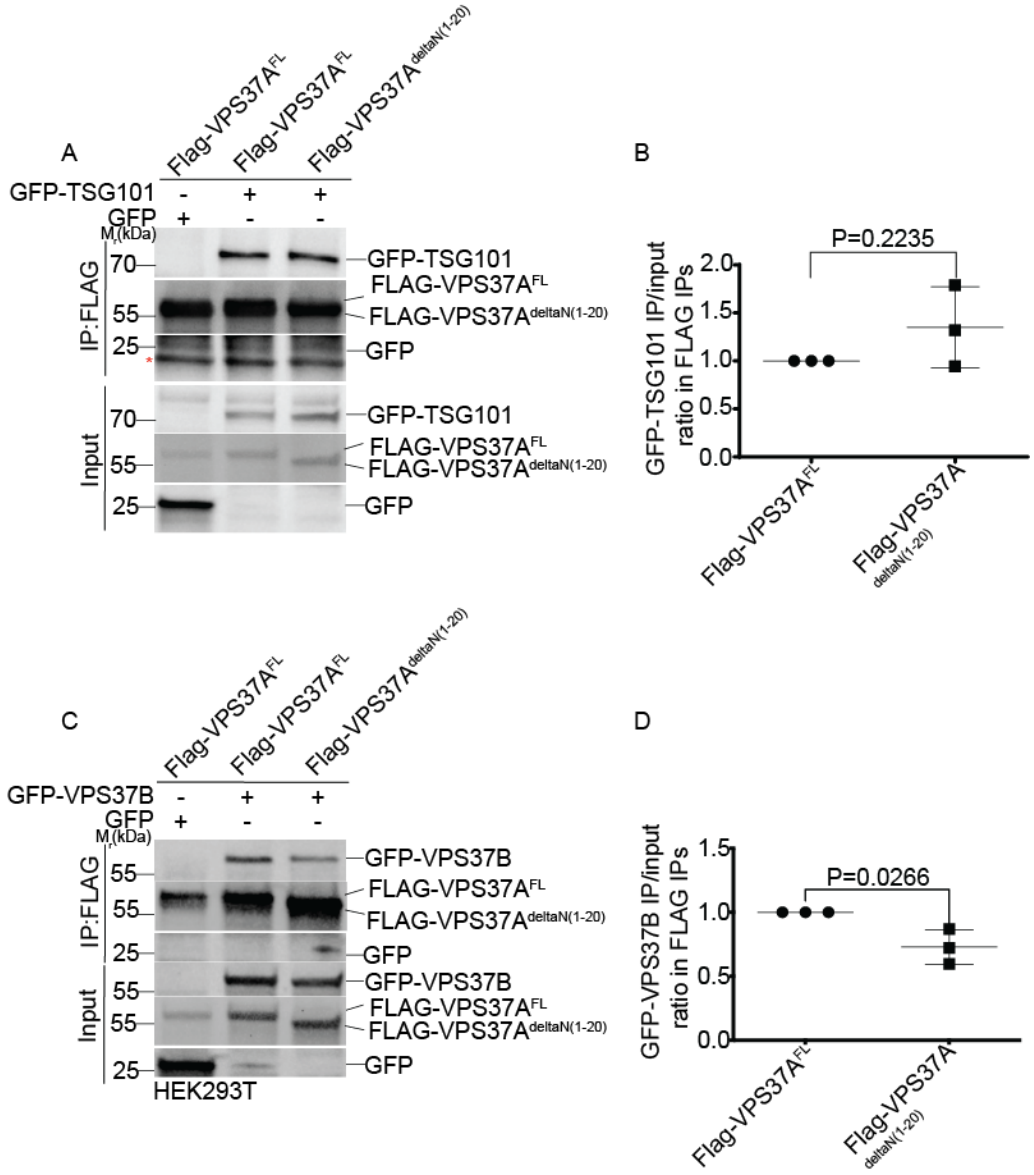

Appendix Figure S5. Effects of N-terminal 20 residues deletion in VPS37A on ESCRT-I complexes.

(A-B) Co-IP analyses in HEK293T cells expressing FLAG-VPS37A^{FL} or VPS37A$^{deltaN(1-20)}$ co-transfected with GFP-TSG101. 5% of input was loaded. (B) Quantification of Co-IP analysis, GFP-TSG101 band intensity ratio (relative to FLAG-VPS37A input in FLAG IP). Statistical significance was determined by t-test. All values are means ± SD, n = 3 biologically independent replicates. Red asterisk IgG light chain band.

(C-D) Co-IP analyses of GFP-VPS37B in HEK293T cells expressing FLAG-VPS37A^{FL}, VPS37A$^{deltaN(1-20)}$ and co-transfected with GFP-VPS37B. 5% of input was loaded. (D) Quantification of Co-IP analysis, GFP-VPS37B band intensity ratio (relative to FLAG-VPS37A input in FLAG IP). Statistical significance was determined by t-test. All values are means ± SD, n = 3 biologically independent replicates.